10-2015

Study of dynamics of $D^0 \to K^- e^+ \nu e$ and $D^0 \to \pi^- e^+ \nu e$ decays

Onur Albayrak
Carnegie Mellon University

Jake V. Bennett
Carnegie Mellon University, jvbennett@cmu.edu

Roy A. Briere
Carnegie Mellon University, rbriere@andrew.cmu.edu

B. C. Ke
Carnegie Mellon University

C. L. Liu
Carnegie Mellon University

See next page for additional authors

Published In
Physical Review D, 92, 7, 072012.

Study of dynamics of $D^0 \to K^- e^+ \nu_e$ and $D^0 \to \pi^- e^+ \nu_e$ decays

M. Ablikim,[1] M. N. Achasov,[9,f] X. C. Ai,[1] O. Albayrak,[5] M. Albrecht,[4] D. J. Ambrose,[44] A. Amoroso,[49a,49c] F. F. An,[1] Q. An,[46,a] J. Z. Bai,[1] R. Baldini Ferroli,[20a] Y. Ban,[31] D. W. Bennett,[19] J. V. Bennett,[5] M. Bertani,[20a] D. Bettoni,[21a] J. M. Bian,[43] F. Bianchi,[49a,49c] E. Boger,[23,d] I. Boyko,[23] R. A. Briere,[5] H. Cai,[51] X. Cai,[1,a] O. Cakir,[40a,b] A. Calcaterra,[20a] G. F. Cao,[1] S. A. Cetin,[40b] J. F. Chang,[1,a] G. Chelkov,[23,d,e] G. Chen,[1] H. S. Chen,[1] H. Y. Chen,[2] J. C. Chen,[1] M. L. Chen,[1,a] S. J. Chen,[29] X. Chen,[1,a] X. R. Chen,[26] Y. B. Chen,[1,a] H. P. Cheng,[17] X. K. Chu,[31] G. Cibinetto,[21a] H. L. Dai,[1,a] J. P. Dai,[34] A. Dbeyssi,[14] D. Dedovich,[23] Z. Y. Deng,[1] A. Denig,[22] I. Denysenko,[23] M. Destefanis,[49a,49c] F. De Mori,[49a,49c] Y. Ding,[27] C. Dong,[30] J. Dong,[1,a] L. Y. Dong,[1] M. Y. Dong,[1,a] S. X. Du,[53] P. F. Duan,[1] E. E. Eren,[40b] J. Z. Fan,[39] J. Fang,[1,a] S. S. Fang,[1] X. Fang,[46,a] Y. Fang,[1] L. Fava,[49b,49c] F. Feldbauer,[22] G. Felici,[20a] C. Q. Feng,[46,a] E. Fioravanti,[21a] M. Fritsch,[14,22] C. D. Fu,[1] Q. Gao,[1] X. Y. Gao,[2] Y. Gao,[39] Z. Gao,[46,a] I. Garzia,[21a] K. Goetzen,[10] W. X. Gong,[1,a] W. Gradl,[22] M. Greco,[49a,49c] M. H. Gu,[1,a] Y. T. Gu,[12] Y. H. Guan,[1] A. Q. Guo,[1] L. B. Guo,[28] Y. Guo,[1] Y. P. Guo,[22] Z. Haddadi,[25] A. Hafner,[22] S. Han,[51] X. Q. Hao,[15] F. A. Harris,[42] K. L. He,[1] X. Q. He,[45] T. Held,[4] Y. K. Heng,[1,a] Z. L. Hou,[1] C. Hu,[28] H. M. Hu,[1] J. F. Hu,[49a,49c] T. Hu,[1,a] Y. Hu,[1] G. M. Huang,[6] G. S. Huang,[46,a] J. S. Huang,[15] X. T. Huang,[33] Y. Huang,[29] T. Hussain,[48] Q. Ji,[1] Q. P. Ji,[30] X. B. Ji,[1] X. L. Ji,[1,a] L. L. Jiang,[1] L. W. Jiang,[51] X. S. Jiang,[1,a] X. Y. Jiang,[30] J. B. Jiao,[33] Z. Jiao,[17] D. P. Jin,[1,a] S. Jin,[1] T. Johansson,[50] A. Julin,[43] N. Kalantar-Nayestanaki,[25] X. L. Kang,[1] X. S. Kang,[30] M. Kavatsyuk,[25] B. C. Ke,[5] P. Kiese,[22] R. Kliemt,[14] B. Kloss,[22] O. B. Kolcu,[40b,i] B. Kopf,[4] M. Kornicer,[42] W. Kuehn,[24] A. Kupsc,[50] J. S. Lange,[24] M. Lara,[19] P. Larin,[14] C. Leng,[49c] C. Li,[50] Cheng Li,[46,a] D. M. Li,[53] F. Li,[1,a] F. Y. Li,[31] G. Li,[1] H. B. Li,[1] J. C. Li,[1] Jin Li,[32] K. Li,[33] K. Li,[13] Lei Li,[3] P. R. Li,[41] T. Li,[33] W. D. Li,[1] W. G. Li,[1] X. L. Li,[33] X. M. Li,[12] X. N. Li,[1,a] X. Q. Li,[30] Z. B. Li,[38] H. Liang,[46,a] Y. F. Liang,[36] Y. T. Liang,[24] G. R. Liao,[11] D. X. Lin,[14] B. J. Liu,[1] C. L. Liu,[5] C. X. Liu,[1] F. H. Liu,[35] Fang Liu,[1] Feng Liu,[6] H. B. Liu,[12] H. H. Liu,[16] H. H. Liu,[1] H. M. Liu,[1] J. Liu,[1] J. B. Liu,[46,a] J. P. Liu,[51] J. Y. Liu,[1] K. Liu,[39] K. Y. Liu,[27] L. D. Liu,[31] P. L. Liu,[1,a] Q. Liu,[41] S. B. Liu,[46,a] X. Liu,[26] Y. B. Liu,[30] Z. A. Liu,[1,a] Zhiqing Liu,[22] H. Loehner,[25] X. C. Lou,[1,a,h] H. J. Lu,[17] J. G. Lu,[1,a] Y. Lu,[1] Y. P. Lu,[1,a] C. L. Luo,[28] M. X. Luo,[52] T. Luo,[42] X. L. Luo,[1,a] X. R. Lyu,[41] F. C. Ma,[27] H. L. Ma,[1] L. L. Ma,[33] Q. M. Ma,[1] T. Ma,[1] X. N. Ma,[30] X. Y. Ma,[1,a] F. E. Maas,[14] M. Maggiora,[49a,49c] Y. J. Mao,[31] Z. P. Mao,[1] S. Marcello,[49a,49c] J. G. Messchendorp,[25] J. Min,[1,a] R. E. Mitchell,[19] X. H. Mo,[1,a] Y. J. Mo,[6] C. Morales Morales,[14] K. Moriya,[19] N. Yu. Muchnoi,[9,f] H. Muramatsu,[43] Y. Nefedov,[23] F. Nerling,[14] I. B. Nikolaev,[9,f] Z. Ning,[1,a] S. Nisar,[8] S. L. Niu,[1,a] X. Y. Niu,[1] S. L. Olsen,[32] Q. Ouyang,[1,a] S. Pacetti,[20b] P. Patteri,[20a] M. Pelizaeus,[4] H. P. Peng,[46,a] K. Peters,[10] J. Pettersson,[50] J. L. Ping,[28] R. G. Ping,[1] R. Poling,[43] V. Prasad,[1] M. Qi,[29] S. Qian,[1,a] C. F. Qiao,[41] L. Q. Qin,[33] N. Qin,[51] X. S. Qin,[1] Z. H. Qin,[1,a] J. F. Qiu,[1] K. H. Rashid,[48] C. F. Redmer,[22] M. Ripka,[22] G. Rong,[1,j] Ch. Rosner,[14] X. D. Ruan,[12] V. Santoro,[21a] A. Sarantsev,[23,g] M. Savrié,[21b] K. Schoenning,[50] S. Schumann,[22] W. Shan,[31] M. Shao,[46,a] C. P. Shen,[2] P. X. Shen,[30] X. Y. Shen,[1] H. Y. Sheng,[1] W. M. Song,[1] X. Y. Song,[1] S. Sosio,[49a,49c] S. Spataro,[49a,49c] G. X. Sun,[1] J. F. Sun,[15] S. S. Sun,[1] Y. J. Sun,[46,a] Y. Z. Sun,[1] Z. J. Sun,[1,a] Z. T. Sun,[19] C. J. Tang,[36] X. Tang,[1] I. Tapan,[40c] E. H. Thorndike,[44] M. Tiemens,[25] M. Ullrich,[24] I. Uman,[40b] G. S. Varner,[42] B. Wang,[30] D. Wang,[31] D. Y. Wang,[31] K. Wang,[1,a] L. L. Wang,[1] L. S. Wang,[1] M. Wang,[33] P. Wang,[1] P. L. Wang,[1] S. G. Wang,[31] W. Wang,[1,a] X. F. Wang,[39] Y. D. Wang,[14] Y. F. Wang,[1,a] Y. Q. Wang,[22] Z. Wang,[1,a] Z. G. Wang,[1,a] Z. H. Wang,[46,a] Z. Y. Wang,[1] T. Weber,[22] D. H. Wei,[11] J. B. Wei,[31] P. Weidenkaff,[22] S. P. Wen,[1] U. Wiedner,[4] M. Wolke,[50] L. H. Wu,[1] Z. Wu,[1,a] L. G. Xia,[39] Y. Xia,[18] D. Xiao,[1] H. Xiao,[47] Z. J. Xiao,[28] Y. G. Xie,[1,a] Q. L. Xiu,[1,a] G. F. Xu,[1] L. Xu,[1] Q. J. Xu,[13] X. P. Xu,[37] L. Yan,[46,a] W. B. Yan,[46,a] W. C. Yan,[46,a] Y. H. Yan,[18] H. J. Yang,[34] H. X. Yang,[1] L. Yang,[51] Y. Yang,[6] Y. X. Yang,[11] M. Ye,[1,a] M. H. Ye,[7] J. H. Yin,[1] B. X. Yu,[1,a] C. X. Yu,[30] J. S. Yu,[26] C. Z. Yuan,[1] W. L. Yuan,[29] Y. Yuan,[1] A. Yuncu,[40b,c] A. A. Zafar,[48] A. Zallo,[20a] Y. Zeng,[18] B. X. Zhang,[1] B. Y. Zhang,[1,a] C. Zhang,[29] C. C. Zhang,[1] D. H. Zhang,[1] H. H. Zhang,[38] H. Y. Zhang,[1,a] J. J. Zhang,[1] J. L. Zhang,[1] J. Q. Zhang,[1] J. W. Zhang,[1,a] J. Y. Zhang,[1] J. Z. Zhang,[1] K. Zhang,[1] L. Zhang,[1] X. Y. Zhang,[33] Y. Zhang,[1] Y. N. Zhang,[41] Y. H. Zhang,[1,a] Y. T. Zhang,[46,a] Yu Zhang,[41] Z. H. Zhang,[6] Z. P. Zhang,[46] Z. Y. Zhang,[51] G. Zhao,[1] J. W. Zhao,[1,a] J. Y. Zhao,[1] J. Z. Zhao,[1,a] Lei Zhao,[46,a] Ling Zhao,[1] M. G. Zhao,[30] Q. Zhao,[1] Q. W. Zhao,[1] S. J. Zhao,[53] T. C. Zhao,[1] Y. B. Zhao,[1,a] Z. G. Zhao,[46,a] A. Zhemchugov,[23,d] B. Zheng,[47] J. P. Zheng,[1,a] W. J. Zheng,[33] Y. H. Zheng,[41] B. Zhong,[28] L. Zhou,[1,a] X. Zhou,[51] X. K. Zhou,[46,a] X. R. Zhou,[46,a] X. Y. Zhou,[1] K. Zhu,[1] K. J. Zhu,[1,a] S. Zhu,[1] S. H. Zhu,[45] X. L. Zhu,[39] Y. C. Zhu,[46,a] Y. S. Zhu,[1] Z. A. Zhu,[1] J. Zhuang,[1,a] L. Zotti,[49a,49c] B. S. Zou,[1] and J. H. Zou[1]

(BESIII Collaboration)

[1]*Institute of High Energy Physics, Beijing 100049, People's Republic of China*
[2]*Beihang University, Beijing 100191, People's Republic of China*
[3]*Beijing Institute of Petrochemical Technology, Beijing 102617, People's Republic of China*
[4]*Bochum Ruhr-University, D-44780 Bochum, Germany*

[5]*Carnegie Mellon University, Pittsburgh, Pennsylvania 15213, USA*
[6]*Central China Normal University, Wuhan 430079, People's Republic of China*
[7]*China Center of Advanced Science and Technology, Beijing 100190, People's Republic of China*
[8]*COMSATS Institute of Information Technology, Lahore, Defence Road, Off Raiwind Road, 54000 Lahore, Pakistan*
[9]*G.I. Budker Institute of Nuclear Physics SB RAS (BINP), Novosibirsk 630090, Russia*
[10]*GSI Helmholtzcentre for Heavy Ion Research GmbH, D-64291 Darmstadt, Germany*
[11]*Guangxi Normal University, Guilin 541004, People's Republic of China*
[12]*GuangXi University, Nanning 530004, People's Republic of China*
[13]*Hangzhou Normal University, Hangzhou 310036, People's Republic of China*
[14]*Helmholtz Institute Mainz, Johann-Joachim-Becher-Weg 45, D-55099 Mainz, Germany*
[15]*Henan Normal University, Xinxiang 453007, People's Republic of China*
[16]*Henan University of Science and Technology, Luoyang 471003, People's Republic of China*
[17]*Huangshan College, Huangshan 245000, People's Republic of China*
[18]*Hunan University, Changsha 410082, People's Republic of China*
[19]*Indiana University, Bloomington, Indiana 47405, USA*
[20a]*INFN Laboratori Nazionali di Frascati, I-00044 Frascati, Italy*
[20b]*INFN and University of Perugia, I-06100 Perugia, Italy*
[21a]*INFN Sezione di Ferrara, I-44122 Ferrara, Italy*
[21b]*University of Ferrara, I-44122 Ferrara, Italy*
[22]*Johannes Gutenberg University of Mainz, Johann-Joachim-Becher-Weg 45, D-55099 Mainz, Germany*
[23]*Joint Institute for Nuclear Research, 141980 Dubna, Moscow region, Russia*
[24]*Justus Liebig University Giessen, II. Physikalisches Institut, Heinrich-Buff-Ring 16, D-35392 Giessen, Germany*
[25]*KVI-CART, University of Groningen, NL-9747 AA Groningen, Netherlands*
[26]*Lanzhou University, Lanzhou 730000, People's Republic of China*
[27]*Liaoning University, Shenyang 110036, People's Republic of China*
[28]*Nanjing Normal University, Nanjing 210023, People's Republic of China*
[29]*Nanjing University, Nanjing 210093, People's Republic of China*
[30]*Nankai University, Tianjin 300071, People's Republic of China*
[31]*Peking University, Beijing 100871, People's Republic of China*
[32]*Seoul National University, Seoul, 151-747 Korea*
[33]*Shandong University, Jinan 250100, People's Republic of China*
[34]*Shanghai Jiao Tong University, Shanghai 200240, People's Republic of China*
[35]*Shanxi University, Taiyuan 030006, People's Republic of China*
[36]*Sichuan University, Chengdu 610064, People's Republic of China*
[37]*Soochow University, Suzhou 215006, People's Republic of China*
[38]*Sun Yat-Sen University, Guangzhou 510275, People's Republic of China*
[39]*Tsinghua University, Beijing 100084, People's Republic of China*
[40a]*Istanbul Aydin University, 34295 Sefakoy, Istanbul, Turkey*
[40b]*Dogus University, 34722 Istanbul, Turkey*
[40c]*Uludag University, 16059 Bursa, Turkey*
[41]*University of Chinese Academy of Sciences, Beijing 100049, People's Republic of China*
[42]*University of Hawaii, Honolulu, Hawaii 96822, USA*
[43]*University of Minnesota, Minneapolis, Minnesota 55455, USA*
[44]*University of Rochester, Rochester, New York 14627, USA*
[45]*University of Science and Technology Liaoning, Anshan 114051, People's Republic of China*
[46]*University of Science and Technology of China, Hefei 230026, People's Republic of China*
[47]*University of South China, Hengyang 421001, People's Republic of China*
[48]*University of the Punjab, Lahore-54590, Pakistan*
[49a]*University of Turin, I-10125 Turin, Italy*
[49b]*University of Eastern Piedmont, I-15121 Alessandria, Italy*
[49c]*INFN, I-10125 Turin, Italy*
[50]*Uppsala University, Box 516, SE-75120 Uppsala, Sweden*

[51]Wuhan University, Wuhan 430072, People's Republic of China
[52]Zhejiang University, Hangzhou 310027, People's Republic of China
[53]Zhengzhou University, Zhengzhou 450001, People's Republic of China
(Received 30 August 2015; published 22 October 2015)

In an analysis of a 2.92 fb^{-1} data sample taken at 3.773 GeV with the BESIII detector operated at the BEPCII collider, we measure the absolute decay branching fractions $\mathcal{B}(D^0 \to K^- e^+ \nu_e) = (3.505 \pm 0.014 \pm 0.033)\%$ and $\mathcal{B}(D^0 \to \pi^- e^+ \nu_e) = (0.295 \pm 0.004 \pm 0.003)\%$. From a study of the differential decay rates we obtain the products of hadronic form factor and the magnitude of the Cabibbo-Kobayashi-Maskawa (CKM) matrix element $f_+^K(0)|V_{cs}| = 0.7172 \pm 0.0025 \pm 0.0035$ and $f_+^\pi(0)|V_{cd}| = 0.1435 \pm 0.0018 \pm 0.0009$. Combining these products with the values of $|V_{cs(d)}|$ from the SM constraint fit, we extract the hadronic form factors $f_+^K(0) = 0.7368 \pm 0.0026 \pm 0.0036$ and $f_+^\pi(0) = 0.6372 \pm 0.0080 \pm 0.0044$, and their ratio $f_+^\pi(0)/f_+^K(0) = 0.8649 \pm 0.0112 \pm 0.0073$. These form factors and their ratio are used to test unquenched lattice QCD calculations of the form factors and a light cone sum rule (LCSR) calculation of their ratio. The measured value of $f_+^{K(\pi)}(0)|V_{cs(d)}|$ and the lattice QCD value for $f_+^{K(\pi)}(0)$ are used to extract values of the CKM matrix elements of $|V_{cs}| = 0.9601 \pm 0.0033 \pm 0.0047 \pm 0.0239$ and $|V_{cd}| = 0.2155 \pm 0.0027 \pm 0.0014 \pm 0.0094$, where the third errors are due to the uncertainties in lattice QCD calculations of the form factors. Using the LCSR value for $f_+^\pi(0)/f_+^K(0)$, we determine the ratio $|V_{cd}|/|V_{cs}| = 0.238 \pm 0.004 \pm 0.002 \pm 0.011$, where the third error is from the uncertainty in the LCSR normalization. In addition, we measure form factor parameters for three different theoretical models that describe the weak hadronic charged currents for these two semileptonic decays. All of these measurements are the most precise to date.

DOI: 10.1103/PhysRevD.92.072012 PACS numbers: 13.20.Fc, 12.15.Hh

I. INTRODUCTION

In the Standard Model (SM) of particle physics, the mixing between the quark flavors in the weak interaction is parametrized by the unitary 3×3 Cabibbo-Kobayashi-Maskawa (CKM) matrix $\hat{V}_{\rm CKM}$ [1,2]. The CKM matrix elements are fundamental parameters of the SM, which have to be measured in experiments. Beyond the SM, some New Physics (NP) effects could also be involved in the weak interactions of the quark flavors, and modify the coupling strength of the quark flavor transitions. Due to these two reasons, precise measurements of the CKM matrix elements are very important for many tests of the SM and searches for NP beyond the SM. Each CKM matrix element can be extracted from measurements of different processes supplemented by theoretical calculations of corresponding hadronic matrix elements. Since the effects of the strong and weak interactions can be well separated in semileptonic $D^0 \to K^- e^+ \nu_e$ and $D^0 \to \pi^- e^+ \nu_e$ decays, these processes are well suited for the determination of the magnitudes of the CKM matrix elements V_{cs} and V_{cd}, and also for studies of the weak decay mechanisms of charmed mesons. If any significant inconsistency between the precise direct measurements of $|V_{cd}|$ or $|V_{cs}|$ and those obtained from the SM global fit is observed, it may indicate that some NP effects are involved in the first two quark generations [3].

In the limit of zero positron mass, the differential rate for $D^0 \to K^-(\pi^-) e^+ \nu_e$ decay is given by

$$\frac{d\Gamma}{dq^2} = \frac{G_F^2}{24\pi^3} |V_{cs(d)}|^2 |\vec{p}_{K^-(\pi^-)}|^3 |f_+^{K(\pi)}(q^2)|^2, \qquad (1.1)$$

where G_F is the Fermi coupling constant, $\vec{p}_{K^-(\pi^-)}$ is the three-momentum of the $K^-(\pi^-)$ meson in the rest frame of the D^0 meson, and $f_+^{K(\pi)}(q^2)$ represents the hadronic form factors of the hadronic weak current that depend on the square of the four-momentum transfer $q = p_{D^0} - p_{K^-(\pi^-)}$. These form factors describe strong interaction effects that can be calculated in lattice quantum chromodynamics (LQCD).

In recent years, LQCD has provided calculations of these form factors with steadily increasing precision. With these

[a]Also at State Key Laboratory of Particle Detection and Electronics, Beijing 100049, Hefei 230026, People's Republic of China.
[b]Also at Ankara University, 06100 Tandogan, Ankara, Turkey.
[c]Also at Bogazici University, 34342 Istanbul, Turkey.
[d]Also at the Moscow Institute of Physics and Technology, Moscow 141700, Russia.
[e]Also at the Functional Electronics Laboratory, Tomsk State University, Tomsk, 634050, Russia.
[f]Also at the Novosibirsk State University, Novosibirsk, 630090, Russia.
[g]Also at the NRC Kurchatov Institute, PNPI, 188300, Gatchina, Russia.
[h]Also at University of Texas at Dallas, Richardson, Texas 75083, USA.
[i]Also at Istanbul Arel University, 34295 Istanbul, Turkey.
[j]Corresponding author.
rongg@ihep.ac.cn

improvements in precision, experimental validation of the computed results are more and more important. At present, the main uncertainty of the apex of the B_d unitarity triangle (UT) of B meson decays is dominated by the theoretical errors in the LQCD determinations of the B meson decay constants $f_{B_{(s)}}$ and decay form factor $f_+^{B\to\pi}(0)$ [3]. Precision measurements of the charmed-sector form factors $f_+^{K(\pi)}(q^2)$ can be used to establish the level of reliability of LQCD calculations of $f_+^{B\to\pi}(0)$. If the LQCD calculations of $f_+^{K(\pi)}(q^2)$ agree well with measured $f_+^{K(\pi)}(q^2)$ values, the LQCD calculations of the form factors for B meson semileptonic decays can be more confidently used to improve measurements of B meson semileptonic decay rates. The improved measurements of B meson semileptonic decay rates would, in turn, improve the determination of the B_d unitarity triangle, with which one can more precisely test the SM and search for NP.

In this paper, we present direct measurements of the absolute branching fractions for $D^0 \to K^- e^+ \nu_e$ and $D^0 \to \pi^- e^+ \nu_e$ decays using a 2.92 fb^{-1} data sample taken at 3.773 GeV with the BESIII detector [4] operated at the upgraded Beijing Electron Positron Collider (BEPCII) [5]. (Throughout this paper, the inclusion of charge conjugate channels is implied.) By analyzing partial decay rates for $D^0 \to K^- e^+ \nu_e$ and $D^0 \to \pi^- e^+ \nu_e$, we obtain the q^2 dependence of the form factors $f_+^{K(\pi)}(q^2)$. Furthermore we extract the form factors $f_+^K(0)$ and $f_+^\pi(0)$ using values of $|V_{cs}|$ and $|V_{cd}|$ determined by the CKMfitter group [6]. Conversely, taking LQCD values for $f_+^K(0)$ and $f_+^\pi(0)$ as inputs, we determine the values of the CKM matrix elements $|V_{cs}|$ and $|V_{cd}|$.

We review the approaches for describing the dynamics of $D^0 \to K^- e^+ \nu_e$ and $D^0 \to \pi^- e^+ \nu_e$ decays in Sec. II. We then describe the BESIII detector, the data sample and the simulated Monte Carlo events used in this analysis in Sec. III. In Sec. IV, we introduce the analysis technique used to identify the semileptonic decay events. The measurements of the absolute branching fractions for these two decays and study of systematic uncertainties in these branching fraction measurements are described in Sec. V. In Sec. VI, we describe the analysis techniques for measuring the differential decay rates for these two semileptonic decays, and present our measurements of the hadronic form factors. The determinations of the CKM matrix elements $|V_{cs}|$ and $|V_{cd}|$ are discussed in Sec. VII. We give a summary of our measurements in Sec. VIII.

II. FORM FACTOR AND APPROACHES FOR D^0 SEMILEPTONIC DECAYS

A. Hadronic form factor

In general, the form factor $f_+^{K(\pi)}(q^2)$ can be expressed in terms of a dispersion relation [7]

$$f_+(q^2) = \frac{f_+(0)/(1-\lambda)}{1-\frac{q^2}{M_{\rm pole}^2}} + \frac{1}{\pi}\int_{t_+}^{\infty} dt \frac{{\rm Im} f_+(t)}{t-q^2-i\epsilon}, \quad (2.1)$$

where $M_{\rm pole}$ is the mass of the lowest-lying relevant vector meson, for $D^0 \to K^- e^+ \nu_e$ it is the D_s^{*+}, while for $D^0 \to \pi^- e^+ \nu_e$ it is the D^{*+}, $f_+(0)$ is the form factor evaluated at the four-momentum transfer $q = 0$, λ is the relative size of the contribution to $f_+(0)$ from the vector pole at $q^2 = 0$, $t_+ = (m_{D^0} + m_{K^-(\pi^-)})^2$ corresponds to the threshold for $D^0 K^-(\pi^-)$ production, m_{D^0} and $m_{K^-(\pi^-)}$ are the masses of the D^0 and charged kaon (pion) meson, respectively. From Eq. (2.1) we find that, except for the pole position of the lowest-lying meson being located below threshold, $f_+(q^2)$ is analytic outside of a cut in the complex q^2-plane extending along the real axis from t_+ to ∞, corresponding to the production region for the states with the appropriate quantum numbers.

B. Parametrizations of form factor

The form of the dispersion relation given in Eq. (2.1) is often parametrized by keeping the lowest-lying meson pole explicitly and approximating the remaining dispersion integral in Eq. (2.1) by a number of effective poles [7,8]

$$f_+(q^2) = \frac{f_+(0)/(1-\lambda)}{1-\frac{q^2}{M_{\rm pole}^2}} + \frac{1}{\pi}\sum_{k=1}^{N} \frac{\rho_k}{1-\frac{1}{\gamma_k}\frac{q^2}{M_{\rm pole}^2}}, \quad (2.2)$$

where ρ_k and γ_k are expansion parameters that are not predicted. The form factor can be approximated by introducing arbitrarily many effective poles. Equation (2.2) is the starting point for many proposed form factor parametrizations.

1. Single pole form

In the constituent quark model, lattice gauge calculations, and QCD sum rules, such as the Körner-Schuler [9] and Bauer-Stech-Wirbel [10] models, a commonly used form factor has a single pole of the form

$$f_+(q^2) = \frac{f_+(0)}{1-\frac{q^2}{M_{\rm pole}^2}}, \quad (2.3)$$

which is simply the first term in Eq. (2.2) (taking $\lambda = 0$). The pole mass $M_{\rm pole}$ is often treated as a free parameter to improve fit quality.

2. Modified pole model

The modified pole model uses $N = 1$ in Eq. (2.2), and the form factor can be expressed as

$$f_+(q^2) = \frac{f_+(0)}{\left(1-\frac{q^2}{M^2_{\rm pole}}\right)\left(1-\alpha\frac{q^2}{M^2_{\rm pole}}\right)}, \quad (2.4)$$

where α is a free parameter. This model is the so-called Becirevic-Kaidalov (BK) parametrization [8] and has been used in many recent lattice calculations and experimental studies for D^0 meson semileptonic decays.

3. Series expansion

The series expansion [7] is the most general parametrization that is consistent with constraints from QCD. It has the form

$$f_+(t) = \frac{1}{P(t)\Phi(t,t_0)}a_0(t_0)\left(1+\sum_{k=1}^{\infty} r_k(t_0)[z(t,t_0)]^k\right), \quad (2.5)$$

where

$$z(t,t_0) = \frac{\sqrt{t_+-t}-\sqrt{t_+-t_0}}{\sqrt{t_+-t}+\sqrt{t_+-t_0}}, \quad (2.6)$$

$$t_- = (m_{D^0}-m_{K^-(\pi^-)})^2, \quad (2.7)$$

$$t_0 = t_+(1-\sqrt{1-t_-/t_+}), \quad (2.8)$$

$a_0(t_0)$ and $r_k(t_0)$ are real coefficients. The function $P(t) = z(t, m^2_{D_s})$ for $D \to K$ and $P(t) = 1$ for $D \to \pi$. Φ is given by

$$\Phi(t,t_0) = \sqrt{\frac{1}{24\pi\chi_V}}\left(\frac{t_+-t}{t_+-t_0}\right)^{1/4}(\sqrt{t_+-t}+\sqrt{t_+})^{-5} \times(\sqrt{t_+-t}+\sqrt{t_+-t_0})(\sqrt{t_+-t}+\sqrt{t_+-t_-})^{3/2} \times(t_+-t)^{3/4}, \quad (2.9)$$

where χ_V can be obtained from dispersion relations using perturbative QCD and depends on the ratio of the s quark mass to the c quark mass, $\xi = m_s/m_c$ [11]. At leading order, with $\xi = 0$,

$$\chi_V = \frac{3}{32\pi^2 m_c^2}. \quad (2.10)$$

The choice of P and Φ is such that

$$a_0^2(t_0)\left(1+\sum_{k=1}^{\infty} r_k^2(t_0)\right) \le 1. \quad (2.11)$$

The z series expansion is model independent and satisfies analyticity and unitarity. In heavy quark effective theory [12] the coefficients r_k in Eq. (2.5) for $D \to \pi e^+\nu_e$ and $B \to \pi\ell^+\nu_\ell$ decays are related. A measurement of the r_k for the decay of $D \to \pi e^+\nu_e$ therefore provides important information to constrain the class of form factors needed to fit the decays of $B \to \pi\ell^+\nu_\ell$, and thereby provides improvements in the determination of the magnitude of the CKM matrix element V_{ub}. However, the validity of the form factor parametrization given in Eq. (2.5) still needs to be checked with experimental data. This is one of the reasons why it is important to precisely measure the form factors $f_+^{K(\pi)}(q^2)$ for $D^0 \to K^-(\pi^-)e^+\nu_e$ decays.

In practical applications, one often takes $k_{\rm max} = 1$ or $k_{\rm max} = 2$ in Eq. (2.5), which gives following two forms of the form factor:

(a) *Series expansion with two parameters* of the form factor is given by

$$f_+(t) = \frac{1}{P(t)\Phi(t,t_0)}a_0(t_0) \times(1+r_1(t_0)[z(t,t_0)]), \quad (2.12)$$

which gives

$$f_+(t) = \frac{1}{P(t)\Phi(t,t_0)}\frac{f_+(0)P(0)\Phi(0,t_0)}{1+r_1(t_0)z(0,t_0)} \times(1+r_1(t_0)[z(t,t_0)]). \quad (2.13)$$

(b) *Series expansion with three parameters* of the form factor is given by

$$f_+(t) = \frac{1}{P(t)\Phi(t,t_0)}a_0(t_0)(1+r_1(t_0)[z(t,t_0)] + r_2(t_0)[z(t,t_0)]^2), \quad (2.14)$$

which gives

$$f_+(t) = \frac{1}{P(t)\Phi(t,t_0)} \times\frac{f_+(0)P(0)\Phi(0,t_0)}{1+r_1(t_0)z(0,t_0)+r_2(t_0)[z(0,t_0)]^2} \times(1+r_1(t_0)[z(t,t_0)]+r_2(t_0)[z(t,t_0)]^2). \quad (2.15)$$

III. DATA SAMPLE AND THE BESIII EXPERIMENT

At $\sqrt{s} = 3.773$ GeV, the $\psi(3770)$ resonance is directly produced via e^+e^- annihilation. About 93% [6] of $\psi(3770)$ decays to $D\bar{D}$ ($D^0\bar{D}^0$, D^+D^-) meson pairs. In addition, the continuum processes $e^+e^- \to q\bar{q}$ ($q = u, d, s$ quark), $e^+e^- \to \tau^+\tau^-$, $e^+e^- \to \gamma_{\rm ISR}J/\psi$, $e^+e^- \to \gamma_{\rm ISR}\psi(3686)$ events are also produced, where $\gamma_{\rm ISR}$ is the radiative photon

in the initial state. The data sample contains a mixture of all these classes of events. In the analysis, we refer to events other than $\psi(3770)$ decays to $D\bar{D}$ as "non-$D\bar{D}$ process" events.

BEPCII [5] is a double-ring e^+e^- collider operating in the center-of-mass energy region between 2.0 and 4.6 GeV. Its design luminosity at 3.78 GeV is 10^{33} cm^{-2} s^{-1} with a beam current of 0.93 A. The peak luminosity of the machine reached 0.65×10^{33} cm^{-2} s^{-1} at $\sqrt{s} =$ 3.773 GeV in April 2011 during the $\psi(3770)$ data taking. BESIII [4] is a general purpose detector operated at the BEPCII. At the BEPCII colliding point, the e^+ and e^- beams collide with a crossing angle of 22 mrad.

The BESIII detector is a cylindrical magnetic detector with a solid angle coverage of 93% of 4π. It consists of five main components. Surrounding the beam pipe, there is a 43-layer main drift chamber (MDC) that provides precise measurements of charged particle trajectories and ionization energy losses (dE/dx) that are used for particle identification. The momentum resolution for charged particles at 1 GeV/c in a 1 T magnetic field is 0.5%, and the specific dE/dx resolution is 6%. Outside of the MDC, a time-of-flight (TOF) system is used for charged particle identification. The TOF consists of a barrel part made of two layers with 88 pieces of 2.4 m long plastic scintillators in each layer, and two end caps with 96 fan-shaped detectors. The TOF time resolution is 80 ps in the barrel, and 110 ps in the end caps, corresponding to a K/π separation better than 2σ for momenta up to 1 GeV/c. An electromagnetic calorimeter (EMC) surrounds the TOF and is made of 6240 CsI(Tl) crystals arranged in a cylindrical shape (barrel) plus two end caps. The EMC is used to measure the energies of photons and electrons. For 1.0 GeV photons, the energy resolution is 2.5% in the barrel and 5.0% in the end caps, and the one-dimensional position resolution is 6 mm in the barrel and 9 mm in the end caps. A superconducting solenoid magnet outside the EMC provides a 1 T magnetic field in the central tracking region of the detector. A muon identification system is placed outside of the detector, consisting of about 1272 m^2 of resistive plate chambers arranged in nine layers in the barrel and eight layers in the end caps incorporated in the magnetic flux return iron of the magnetic. The position resolution of the muon chambers is about 2 cm. This system efficiently identifies muons with momentum greater than 500 MeV/c over 88% of the total solid angle.

The BESIII detector response was studied using Monte Carlo event samples generated with a GEANT4-based [13] detector simulation software package, BOOST [14]. To match the data, 1.98×10^8 Monte Carlo events for $e^+e^- \to \psi(3770) \to D\bar{D}$ were simulated with the Monte Carlo event generator $\mathcal{KK}$, KKMC [15], where 56% of the $\psi(3770)$ resonance is set to decay to $D^0\bar{D}^0$ while the remainder decays to D^+D^- meson pairs. All of these $D^0\bar{D}^0$ and D^+D^- meson pairs are set to decay into different final states which were generated with EVTGEN [16] with branching fractions from the Particle Data Group (PDG) [6]. This Monte Carlo event sample corresponds to about 11 times the luminosity of real data. With these Monte Carlo events, we determine the event selection criteria for the data analysis and study possible background events for the measurement of the $D^0 \to K^-e^+\nu_e$ and $D^0 \to \pi^-e^+\nu_e$ decays. We refer to these Monte Carlo events as "cocktail vs cocktail $D\bar{D}$ process" events.

Since the non-$D\bar{D}$ process events are mixed with the $D\bar{D}$ events in the data sample, we also generate non-$D\bar{D}$ process Monte Carlo events simulated with KKMC [15] and EVTGEN [16] to estimate the number of the background events in the selected $D^0 \to K^-e^+\nu_e$ and $D^0 \to \pi^-e^+\nu_e$ samples.

To estimate the efficiencies, we also generate "signal" Monte Carlo events, i.e. $\psi(3770) \to D^0\bar{D}^0$ events in which the $\bar{D}^0$ meson decays to all possible final states [6], and the D^0 meson decays to a semileptonic or a hadronic decay final state that is being investigated. These Monte Carlo events were all generated and simulated with the software packages mentioned above.

IV. RECONSTRUCTION OF $D^0\bar{D}^0$ DECAY EVENTS

In $\psi(3770)$ resonance decays into $D\bar{D}$ mesons in which a $\bar{D}$ meson is fully reconstructed, all of the remaining tracks and photons in the event must originate from the accompanying D. In these cases, the reconstructed meson is called a single $\bar{D}$ tag. Using the single $\bar{D}^0$ tag sample, the decays of $D^0 \to K^-e^+\nu_e$ and $D^0 \to \pi^-e^+\nu_e$ can be reliably identified from the recoiling tracks in the event. We refer to the event in which the $\bar{D}^0$ meson is reconstructed and a semileptonic D^0 decay is reconstructed from the recoiling tracks as a doubly tagged $D^0\bar{D}^0$ decay event or a double $D^0\bar{D}^0$ tag. With these doubly tagged $D^0\bar{D}^0$ events, the absolute branching fractions and the differential decay rates for D^0 semileptonic decays can be well measured.

In the analysis, all four-momentum vectors measured in the laboratory frame are boosted to the e^+e^- center-of-mass frame.

In this section, we describe the procedure for selecting the single $\bar{D}^0$ tags and the D^0 semileptonic decay events.

A. Properties of doubly tagged $D^0\bar{D}^0$ decays

For a specific tag decay mode, the number of the single $\bar{D}^0$ tags is given by

$$N_{\rm tag} = 2N_{D^0\bar{D}^0}\mathcal{B}_{\rm tag}\epsilon_{\rm tag}, \tag{4.1}$$

where $N_{D^0\bar{D}^0}$ is the number of the $D^0\bar{D}^0$ meson pairs produced in the data sample, $\mathcal{B}_{\rm tag}$ is the branching fraction for the tag mode, and $\epsilon_{\rm tag}$ is the efficiency for reconstruction

of this mode. Similarly, the number of the D^0 semileptonic decay events observed in the system recoiling against the single $\bar{D}^0$ tags is given by

$$N_{\rm observed}(D^0 \to h^- e^+ \nu_e) = 2N_{D^0\bar{D}^0}\mathcal{B}_{\rm tag}\mathcal{B}(D^0 \to h^- e^+ \nu_e) \times \epsilon_{{\rm tag},D^0\to h^- e^+\nu_e}, \quad (4.2)$$

where h^- denotes the final state hadron (i.e. $h^- = K^-$ or π^-), $\mathcal{B}(D^0 \to h^- e^+ \nu_e)$ is the D^0 meson semileptonic decay branching fraction, and $\epsilon_{{\rm tag},D^0\to h^- e^+\nu_e}$ is the efficiency of simultaneously reconstructing both the single $\bar{D}^0$ tag and the D^0 meson semileptonic decay. With these two equations, we obtain

$$\mathcal{B}(D^0 \to h^- e^+ \nu_e) = \frac{N_{\rm observed}(D^0 \to h^- e^+ \nu_e)}{N_{\rm tag}\epsilon(D^0 \to h^- e^+ \nu_e)}, \quad (4.3)$$

where $\epsilon(D^0 \to h^- e^+ \nu_e) = \epsilon_{{\rm tag},D^0\to h^- e^+\nu_e}/\epsilon_{\rm tag}$.

To measure the D^0 semileptonic differential decay rates given in Eq. (1.1) we need to evaluate the partial decay rate $\Delta\Gamma_i$ observed within a small range of the squared four-momentum transfer Δq_i^2, where i stands for the ith q^2 bin. This partial decay rate can be evaluated with the double tag $D^0\bar{D}^0$ events as well. The measurement of the partial decay rates is described in Sec. VI.

B. Single $\bar{D}^0$ tags and efficiencies

The $\bar{D}^0$ meson is reconstructed in five hadronic decay modes: $K^+\pi^-$, $K^+\pi^-\pi^0$, $K^+\pi^-\pi^-\pi^+$, $K^+\pi^-\pi^+\pi^-\pi^0$ and $K^+\pi^-\pi^0\pi^0$. Events that contain at least two reconstructed charged tracks with good helix fits are selected. The charged tracks used in the single tag analysis are required to satisfy $|\cos\theta| < 0.93$, where θ is the polar angle of the charged track. All of these charged tracks are required to originate from the interaction region with a distance of closest approach in the transverse plane that is less than 1.0 cm and less than 15.0 cm along the z axis. The dE/dx and TOF measurements are combined to form confidence levels for pion (CL_π) and kaon (CL_K) particle identification hypotheses. In the selection of single $\bar{D}^0$ tags, pion (kaon) identification requires $CL_\pi > CL_K (CL_K > CL_\pi)$ for momenta $p < 0.75$ GeV/c and $CL_\pi > 0.1\%$ ($CL_K > 0.1\%$) for $p \geq 0.75$ GeV/c.

A π^0 meson is reconstructed via the decay $\pi^0 \to \gamma\gamma$. To select photons from π^0 decays, we require an energy deposit in the barrel (end-cap) EMC to be greater than 0.025(0.050) GeV and in-time coincidence with the beam crossing. In addition, the angle between the photon and the nearest charged track is required to be greater than 10°. A one-constraint (1-C) kinematic fit is performed to constrain the invariant mass of $\gamma\gamma$ to the mass of π^0 meson, and $\chi^2 < 50$ is required.

For the $\bar{D}^0 \to K^+\pi^-$ final state, we reduce backgrounds from cosmic rays, Bhabha and dimuon events by requiring the difference of the time of flight of the two charged tracks be less than 5 ns, and the opening angle of the two charged track directions be less than 176 degree. In addition, we require that the sum of the ratio of energy over the momentum of the charged track is less than 1.4.

The single $\bar{D}^0$ tags are selected using beam energy constrained mass of the $Kn\pi$ (where $n = 1$, 2, 3, or 4) combination, which is given by

$$M_{\rm BC} = \sqrt{E_{\rm beam}^2 - |\vec{p}_{Kn\pi}|^2}, \quad (4.4)$$

where $E_{\rm beam}$ is the beam energy and $|\vec{p}_{Kn\pi}|$ is the magnitude of the momentum of the daughter $Kn\pi$ system. We also use the variable $\Delta E \equiv E_{Kn\pi} - E_{\rm beam}$, where $E_{Kn\pi}$ is the energy of the $Kn\pi$ combination computed with the identified charged species. Each $Kn\pi$ combination is subjected to a requirement of energy conservation with $|\Delta E| < (2 \sim 3)\sigma_{E_{Kn\pi}}$, where $\sigma_{E_{Kn\pi}}$ is the standard deviation of the $E_{Kn\pi}$ distribution. For each event, there may be several different charged track (or both charged track and neutral cluster) combinations for each of the five single $\bar{D}^0$ tag modes. If more than one combination satisfies the energy requirement, the combination with the smallest value of $|\Delta E|$ is retained.

The dots with error bars in Fig. 1 show the resulting distributions of $M_{\rm BC}$ for the five single $\bar{D}^0$ tag modes, where the $\bar{D}^0$ meson signals are evident. To determine the

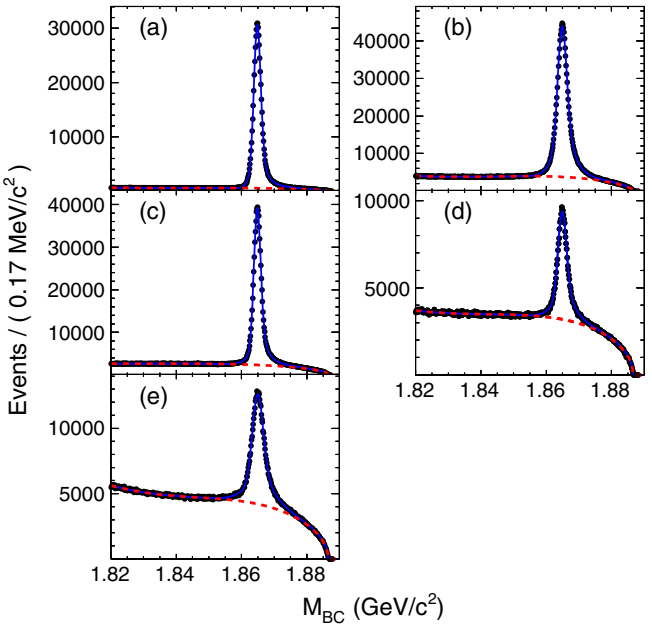

FIG. 1 (color online). Distributions of the beam energy constrained masses of the $Kn\pi$ ($n = 1, 2, 3$ or 4) combinations for the five single $\bar{D}^0$ tag modes: (a) $K^+\pi^-$, (b) $K^+\pi^-\pi^0$, (c) $K^+\pi^-\pi^-\pi^+$, (d) $K^+\pi^-\pi^-\pi^+\pi^0$ and (e) $K^+\pi^-\pi^0\pi^0$.

number of the single $\bar{D}^0$ tags that are reconstructed for each mode, we fit a signal function plus a background shape to these distributions. For the fit, we use signal shapes obtained from Monte Carlo simulation convolved with a double-Gaussian function for the signal component, added to an ARGUS function multiplied by a third-order polynomial function [17,18] to represent the combinatorial background shape. In the Monte Carlo simulation, the effects of beam energy spread, initial state radiation and the $\psi(3770)$ line shape are all taken into account. The ARGUS function is [19]

$$f_{\rm ARGUS}(m) = m\sqrt{1-\left(\frac{m}{E_0}\right)^2}\exp\left[c\left(1-\left(\frac{m}{E_0}\right)^2\right)\right], \tag{4.5}$$

where m is the beam energy constrained mass, E_0 is the end point given by the beam energy and c is a free parameter. The solid lines in Fig. 1 show the best fits, while the dashed lines show the fitted background shapes.

In addition to the combinatorial background, there are also small wrong-sign (WS) peaking backgrounds in single $\bar{D}^0$ tags. The doubly Cabibbo suppressed decays contribute to the WS peaking background for single $\bar{D}^0$ tag modes of $\bar{D}^0 \to K^+\pi^-$, $\bar{D}^0 \to K^+\pi^-\pi^0$ and $\bar{D}^0 \to K^+\pi^-\pi^-\pi^+$. In addition, the $\bar{D}^0 \to K^0_S K^-\pi^+$ $(K^0_S \to \pi^+\pi^-)$, $\bar{D}^0 \to K^0_S K^-\pi^+\pi^0$ $(K^0_S \to \pi^+\pi^-)$ and $K^0_S K^-\pi^+$ $(K^0_S \to \pi^0\pi^0)$ also make significant contributions to WS peaking backgrounds for the $\bar{D}^0 \to K^+\pi^-\pi^-\pi^+$, $\bar{D}^0 \to K^+\pi^-\pi^-\pi^+\pi^0$ and $\bar{D}^0 \to K^+\pi^-\pi^0\pi^0$ tag modes, respectively. The size of these WS peaking backgrounds are estimated from Monte Carlo simulation and then subtracted from the yields obtained from the fits to $M_{\rm BC}$ spectra.

Table I summarizes the single $\bar{D}^0$ tags. In the Table, the second column gives the ΔE requirement on the $Kn\pi$ combination, the fourth column gives the number of the single $\bar{D}^0$ tags in the tag mass region as shown in the third column.

The efficiencies for reconstruction of the single $\bar{D}^0$ tags for the five tag modes are obtained by applying the identical analysis procedure to simulated signal Monte Carlo events mixed with "background" Monte Carlo events. The signal Monte Carlo events are generated as $e^+e^- \to \psi(3770) \to D^0\bar{D}^0$, where the $\bar{D}^0$ meson is set to decay to the tag mode in question and the D^0 meson is set to decay to all possible final states with corresponding branching fractions [6]. The efficiencies for reconstruction of the single $\bar{D}^0$ tags are presented in the last column of Table I.

C. Selection of $D^0 \to K^-e^+\nu_e$ and $D^0 \to \pi^-e^+\nu_e$

The $D^0 \to K^-e^+\nu_e$ and $D^0 \to \pi^-e^+\nu_e$ event candidates are selected from the tracks recoiling against the single $\bar{D}^0$ tags. To select the $D^0 \to K^-e^+\nu_e$ and $D^0 \to \pi^-e^+\nu_e$ events, it is required that there are only two oppositely charged tracks, one of which is identified as a positron and the other as a kaon or a pion. The combined confidence level CL_K (CL_π) for the K (π) hypothesis is required to be greater than CL_π (CL_K) for kaon (pion) candidates. For positron identification, the combined confidence level (CL_e), calculated for the e hypothesis using the dE/dx, TOF and EMC measurements (deposited energy and shape of the electromagnetic shower) is required to be greater than 0.1%, and the ratio $CL_e/(CL_e + CL_\pi + CL_K)$ is required to be greater than 0.8. We include the four-momenta of near-by photons with the direction of the positron momentum to partially account for final-state-radiation energy losses (FSR recovery). In addition, to suppress fake photon background it is required that the maximum energy of any unused photon in the recoil system, $E_{\gamma,\rm max}$, be less than 300 MeV.

Since the neutrino escapes detection, the kinematic variable

$$U_{\rm miss} \equiv E_{\rm miss} - |\vec{p}_{\rm miss}| \tag{4.6}$$

is used to obtain the information about the missing neutrino, where $E_{\rm miss}$ and $\vec{p}_{\rm miss}$ are, respectively, the total missing energy and momentum in the event, computed from

$$E_{\rm miss} = E_{\rm beam} - E_{h^-} - E_{e^+}, \tag{4.7}$$

where E_{h^-} and E_{e^+} are the measured energies of the hadron and the positron, respectively. The $\vec{p}_{\rm miss}$ is calculated by

TABLE I. Summary of the single $\bar{D}^0$ tags and efficiencies for reconstruction of the single $\bar{D}^0$ tags, where ΔE gives the requirements on the energy difference between the measured $E_{Kn\pi}$ and beam energy $E_{\rm beam}$, while the $M_{\rm B}$ range defines the signal region of the single $\bar{D}^0$ tags. $N_{\rm tag}$ is the number of single $\bar{D}^0$ tags and $\epsilon_{\rm tag}$ is the efficiency for reconstruction of the single $\bar{D}^0$ tags, where the uncertainties are only statistical.

Tag mode	ΔE (GeV)	$M_{\rm BC}$ range (GeV/c^2)	$N_{\rm tag}$	$\epsilon_{\rm tag}$ (%)
$K^+\pi^-$	$(-0.049, 0.044)$	(1.860,1.875)	567083 ± 848	70.29 ± 0.07
$K^+\pi^-\pi^0$	$(-0.071, 0.052)$	(1.858,1.875)	1094081 ± 1692	36.80 ± 0.03
$K^+\pi^-\pi^-\pi^+$	$(-0.043, 0.043)$	(1.860,1.875)	700061 ± 1121	39.57 ± 0.04
$K^+\pi^-\pi^-\pi^+\pi^0$	$(-0.067, 0.066)$	(1.858,1.875)	158367 ± 749	15.95 ± 0.08
$K^+\pi^-\pi^0\pi^0$	$(-0.082, 0.050)$	(1.858,1.875)	273725 ± 2859	15.78 ± 0.08
Sum			2793317 ± 3684	

$$\vec{p}_{\rm miss} = \vec{p}_{D^0} - \vec{p}_{h^-} - \vec{p}_{e^+}, \tag{4.8}$$

where $\vec{p}_{D^0}$, $\vec{p}_{h^-}$ and $\vec{p}_{e^+}$ are the momenta of the D^0 meson, the hadron and the positron, respectively. The three-momentum $\vec{p}_{D^0}$ of the D^0 meson is computed by

$$\vec{p}_{D^0} = -\hat{p}_{\rm tag}\sqrt{E^2_{\rm beam} - m^2_{D^0}}, \tag{4.9}$$

where $\hat{p}_{\rm tag}$ is the direction of the momentum of the single $\bar{D}^0$ tag. If the daughter particles from a semileptonic decay are correctly identified, $U_{\rm miss}$ is zero, since only one neutrino is missing.

Figures 2(a) and 2(b) show the $U_{\rm miss}$ distributions for the $D^0 \to K^- e^+ \nu_e$ and $D^0 \to \pi^- e^+ \nu_e$ candidate events, respectively. In both cases, most of the events are from the $D^0 \to K^- e^+ \nu_e$ and $D^0 \to \pi^- e^+ \nu_e$ decays. Backgrounds from $D\bar{D}$ processes include mistagged $\bar{D}^0$ and D^0 decays other than the semileptonic decay in question. Other backgrounds are from non-$D\bar{D}$ process processes. From the simulated cocktail vs cocktail $D\bar{D}$ process events, we find that the $D\bar{D}$ background events are mostly from $D^0 \to K^- \pi^0 e^+ \nu_e$, $D^0 \to K^- \mu^+ \nu_\mu$ and $D^0 \to \pi^- e^+ \nu_e$ selected as $D^0 \to K^- e^+ \nu_e$, and $D^0 \to \pi^- \pi^0 e^+ \nu_e$, $D^0 \to K^- e^+ \nu_\mu$ and $D^0 \to \pi^- \mu^+ \nu_\mu$ selected as $D^0 \to \pi^- e^+ \nu_e$. Backgrounds from non-$D\bar{D}$ processes include the initial state radiation (ISR) return to the $\psi(3686)$ and J/ψ, continuum light hadron production, $\psi(3770) \to$ non-$D\bar{D}$ decays and $e^+e^- \to \tau^+\tau^-$ events. The levels of these backgrounds events are estimated by analyzing the corresponding simulated event samples.

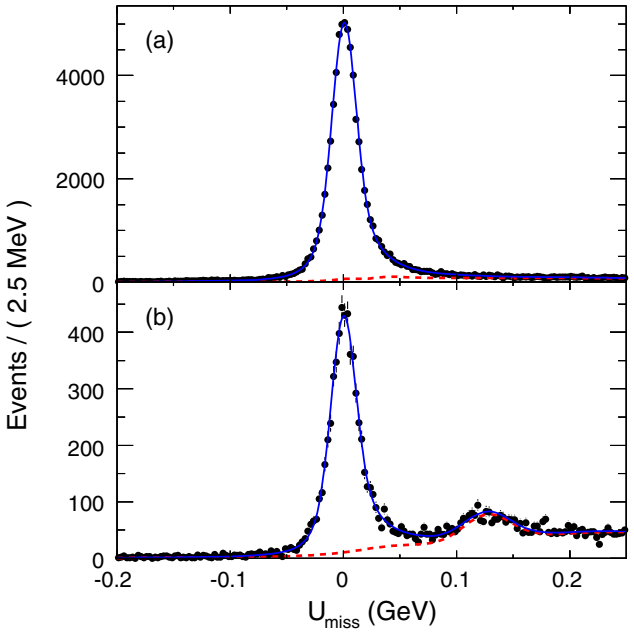

FIG. 2 (color online). $U_{\rm miss}$ distributions of events for (a) $\bar{D}^0$ tags vs $D^0 \to K^- e^+ \nu_e$, and for (b) $\bar{D}^0$ tags vs $D^0 \to \pi^- e^+ \nu_e$, where the dots with error bars show the data, the solid lines show the best fit to the data, and the dashed lines show the background shapes estimated by analyzing the cocktail vs cocktail $D\bar{D}$ process Monte Carlo events and the non-$D\bar{D}$ process Monte Carlo events (see text for more details).

Because of ISR and final state radiation (FSR), the signal $U_{\rm miss}$ distributions are not Gaussian; instead, the $U_{\rm miss}$ distributions have Gaussian cores with long tails at both the lower and the higher sides of the distributions. To obtain the numbers of the signal events for these two semileptonic decays, we fit these distributions with an empirical function that includes these tails.

We use the same probability density function as CLEO [20] for $U_{\rm miss}$,

$$f(x) = \begin{cases} a_1\left(\frac{n_1}{\alpha_1} - \alpha_1 + x\right)^{-n_1} & \text{if } x \geq \alpha_1 \\ \exp(-x^2/2) & \text{if } -\alpha_2 \leq x < \alpha_1 \\ a_2\left(\frac{n_2}{\alpha_2} - \alpha_2 - x\right)^{-n_2} & \text{if } x < -\alpha_2, \end{cases} \tag{4.10}$$

where $x \equiv (U_{\rm miss} - m)/\sigma$, m and σ are the mean value and standard deviation of the Gaussian distribution, respectively. In Eq. (4.10), $a_1 \equiv (n_1/\alpha_1)^{n_1} e^{-\alpha_1^2/2}$, and $a_2 \equiv (n_2/\alpha_2)^{n_2} e^{-\alpha_2^2/2}$, where α_1, α_2, n_1 and n_2 are parameters describing the tails of the signal function, determined from fits to the simulated $U_{\rm miss}$ distributions of signal Monte Carlo events.

To account for differences between data and Monte Carlo, we fit the data using the Monte Carlo determined $f(x)$ distribution convolved with a Gaussian function with free mean and width. The background function is formed from histograms of $U_{\rm miss}$ distributions for background events from the cocktail vs cocktail $D\bar{D}$ and non-$D\bar{D}$ simulated event samples. The normalizations of the signal and background are free parameters in the fits to the data.

The results of the fits to the two $U_{\rm miss}$ distributions are shown in Figs. 2(a) and 2(b); the fitted yields of signal events are

$$N_{\rm observed}(D^0 \to K^- e^+ \nu_e) = 70727 \pm 278 \tag{4.11}$$

and

$$N_{\rm observed}(D^0 \to \pi^- e^+ \nu_e) = 6297 \pm 87. \tag{4.12}$$

In Figs. 2(a) and 2(b), the solid lines show the best fits to the data, while the dashed lines show the background.

To gain confidence in the quality of the Monte Carlo simulation, we examine the momentum distributions of the kaon, the pion and the positron as well as $\cos\theta_{We}$ from the semileptonic decays of $D^0 \to K^- e^+ \nu_e$ and $D^0 \to \pi^- e^+ \nu_e$, where θ_{We} is the angle between the direction of the virtual W^+ boson in the D^0 rest frame and the three-momentum of the positron in the W^+ rest frame. These distributions are

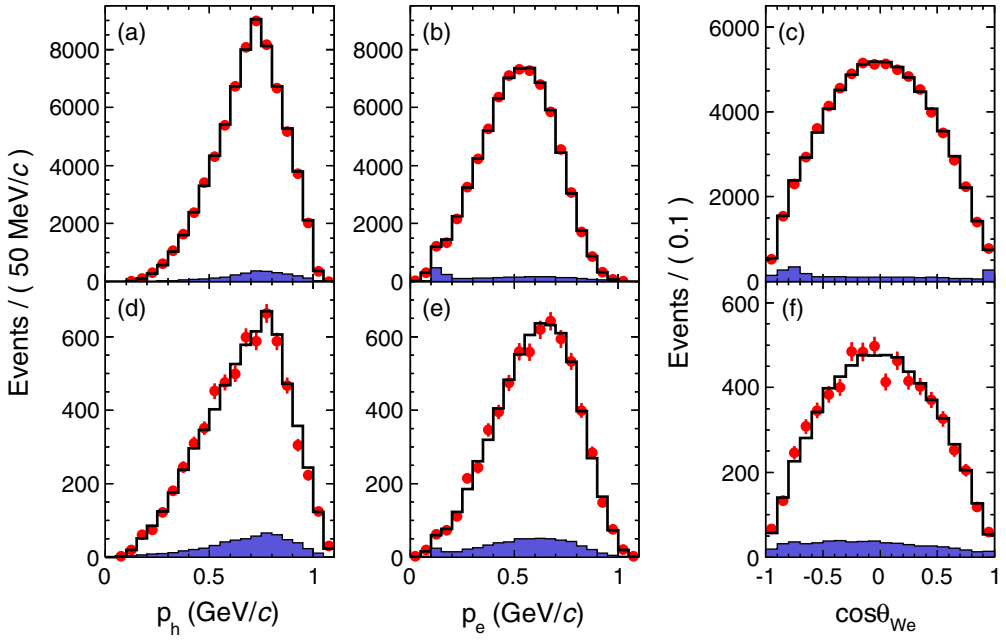

FIG. 3 (color online). Distributions of particle momenta and $\cos\theta_{\rm We}$ from $D^0 \to K^- e^+ \nu_e$ and $D^0 \to \pi^- e^+ \nu_e$ semileptonic decays, where (a) and (b) are the momenta of kaon and positron from $D^0 \to K^- e^+ \nu_e$, respectively; (d) and (e) are the momenta of pion and positron from $D^0 \to \pi^- e^+ \nu_e$, respectively; (c) and (f) are the distributions of $\cos\theta_{\rm We}$ for $D^0 \to K^- e^+ \nu_e$ and $D^0 \to \pi^- e^+ \nu_e$, respectively; these events satisfy $-0.06 < U_{\rm miss} < 0.06$ GeV. The solid histograms are Monte Carlo simulated signal plus background; the shaded histograms are Monte Carlo simulated background only.

shown in Figs. 3(a)–3(f), respectively, where the dots with error bars are for the data, the solid histograms are for the full Monte Carlo simulation and the shaded histograms show the Monte Carlo simulated backgrounds only.

V. MEASUREMENTS OF ABSOLUTE DECAY BRANCHING FRACTIONS

A. Efficiency for reconstruction of semileptonic decays

To determine the efficiency $\epsilon(D^0 \to h^- e^+ \nu_e)$ for reconstruction of each of the two semileptonic decays for each single tag mode, signal Monte Carlo event samples of $\psi(3770) \to D^0 \bar{D}^0$ decays, where the D^0 meson is set to decay to the $h^- e^+ \nu_e$ final state in question and the $\bar{D}^0$ meson is set to decay to each of the five single $\bar{D}^0$ tag modes, are generated and simulated with the BESIII software package. By subjecting these simulated events to the same requirements that are applied to the data we obtain the reconstruction efficiencies $\epsilon_{{\rm tag},D^0 \to h^- e^+ \nu_e}$ for simultaneously finding the D^0 meson semileptonic decay and the single $\bar{D}^0$ tag in the same event; these are given in Table II.

Due to their low multiplicity, it is usually easier to reconstruct $\bar{D}^0$ tags in semileptonic events than in typical $D^0\bar{D}^0$ events (tag bias). In addition, the size of the tag bias is correlated with the multiplicity of the tag mode. In consequence the overall efficiencies shown in Table II vary greatly from the $\bar{D}^0 \to K^-\pi^+$ mode to the $\bar{D}^0 \to K^-\pi^+\pi^+\pi^-$ and $\bar{D}^0 \to K^-\pi^+\pi^0\pi^0$ modes.

The last row in Table II gives the overall efficiency which is obtained by weighting the individual efficiencies for each of the five single $\bar{D}^0$ tags by the corresponding yield shown in Table I.

TABLE II. Double tag efficiencies for reconstruction of "$\bar{D}^0_{\rm tag}$ vs $D^0 \to h^- e^+ \nu_e$" and overall efficiencies for reconstruction of $D^0 \to h^- e^+ \nu_e$ in the recoil side of $\bar{D}^0$ tags, where the uncertainties are only statistical.

Tag mode	$\epsilon_{{\rm tag},D^0 \to K^- e^+ \nu_e}$	$\epsilon_{{\rm tag},D^0 \to \pi^- e^+ \nu_e}$	$\epsilon_{\rm MC}(D^0 \to K^- e^+ \nu_e)$	$\epsilon_{\rm MC}(D^0 \to \pi^- e^+ \nu_e)$
$K^+\pi^-$	0.4566 ± 0.0014	0.4995 ± 0.0014	0.6496 ± 0.0021	0.7106 ± 0.0021
$K^+\pi^-\pi^0$	0.2685 ± 0.0006	0.2927 ± 0.0007	0.7296 ± 0.0017	0.7954 ± 0.0020
$K^+\pi^-\pi^-\pi^+$	0.2666 ± 0.0008	0.2897 ± 0.0008	0.6737 ± 0.0021	0.7321 ± 0.0022
$K^+\pi^-\pi^-\pi^+\pi^0$	0.1260 ± 0.0008	0.1363 ± 0.0008	0.7900 ± 0.0064	0.8545 ± 0.0066
$K^+\pi^-\pi^0\pi^0$	0.1331 ± 0.0007	0.1467 ± 0.0007	0.8435 ± 0.0062	0.9297 ± 0.0065
Average			0.7140 ± 0.0012	0.7788 ± 0.0013

There are small differences in efficiencies for finding a charged particle and for identifying the type of the charged particle between the data and Monte Carlo events that are discussed in Sec. V C. To take these differences into account, the overall efficiencies $\epsilon_{\rm MC}(D^0 \to K^- e^+ \nu_e)$ and $\epsilon_{\rm MC}(D^0 \to \pi^- e^+ \nu_e)$ are corrected by the multiplicative factors of

$$f_{\rm corr}^{\rm trk+PID} = \begin{cases} 1.0118 \pm 0.0050 & \text{for } D^0 \to K^- e^+ \nu_e \\ 0.9814 \pm 0.0040 & \text{for } D^0 \to \pi^- e^+ \nu_e. \end{cases} \quad (5.1)$$

After making these corrections, we obtain the "true" overall efficiencies for reconstruction of these two semileptonic decays,

$$\epsilon(D^0 \to K^- e^+ \nu_e) = 0.7224 \pm 0.0012 \quad (5.2)$$

and

$$\epsilon(D^0 \to \pi^- e^+ \nu_e) = 0.7643 \pm 0.0013, \quad (5.3)$$

where the uncertainties are only statistical.

B. Decay branching fraction

Inserting the number of the single $\bar{D}^0$ tags, the numbers of the signal events for these two D^0 semileptonic decays observed in the recoil of the single $\bar{D}^0$ tags together with corresponding efficiency into Eq. (4.3), we obtain the absolute decay branching fractions

$$\mathcal{B}(D^0 \to K^- e^+ \nu_e) = (3.505 \pm 0.014 \pm 0.033)\% \quad (5.4)$$

and

$$\mathcal{B}(D^0 \to \pi^- e^+ \nu_e) = (0.295 \pm 0.004 \pm 0.003)\%, \quad (5.5)$$

where the first errors are statistical and the second systematic. The sources of systematic uncertainties in the measured decay branching fractions are discussed in the next subsection.

C. Systematic uncertainties in measured branching fractions

Table III lists the sources of the systematic uncertainties in the measured semileptonic branching fractions. We discuss each of these sources in the following.

1. Uncertainty in number of $\bar{D}^0$ tags

To estimate the uncertainty in the number of single $\bar{D}^0$ tags, we repeat the fits to the $M_{\rm BC}$ distributions by varying the bin size, fit range and background functions. We also investigate the contribution arising from possible differences in the π^0 fake rates between data and Monte Carlo simulation. Finally, we assign a systematic uncertainty of 0.5% to the number of $\bar{D}^0$ tags.

TABLE III. Sources of the systematic uncertainties in the measured branching fractions for $D^0 \to K^- e^+ \nu_e$ and $D^0 \to \pi^- e^+ \nu_e$.

Source	Systematic uncertainty (%) $K^- e^+ \nu_e$	$\pi^- e^+ \nu_e$
Number of $\bar{D}^0$ tags	0.50	0.50
Tracking for e^+	0.19	0.15
Tracking for K^-	0.42	···
Tracking for π^-	···	0.28
PID for e^+	0.16	0.14
PID for K^-	0.10	···
PID for π^-	···	0.19
$E_{\gamma,\rm max}$ cut	0.10	0.10
Fit to $U_{\rm miss}$	0.48	0.50
Form factor structure	0.10	0.10
FSR recovery	0.30	0.30
Finite MC statistics	0.17	0.17
Single tag cancelation	0.12	0.12
Total	0.94	0.90

2. Uncertainty in tracking efficiency

The uncertainties for finding a charged track are estimated by comparing the efficiencies for reconstructing the positron, kaon and pion in data and Monte Carlo events.

Using radiative Bhabha scattering events selected from the data and simulated radiative Bhabha scattering events, we measure the difference in efficiencies for finding a positron between data and simulation. Considering both the $\cos\theta$, where θ is the polar angle of the positron, and momentum distributions of the positrons, we obtain two-dimensional weighted-average efficiency differences $(\epsilon_{\rm data}/\epsilon_{\rm MC} - 1)$ of $(0.22 \pm 0.19)\%$ and $(0.11 \pm 0.15)\%$. These translate uncertainties on the decay branching fractions of 0.19% and 0.15% for $D^0 \to K^- e^+ \nu_e$ and $D^0 \to \pi^- e^+ \nu_e$ decays, respectively.

The efficiencies for finding a charged kaon and a charged pion are determined by analyzing doubly tagged $D\bar{D}$ decay events. In the selection of the doubly tagged $D\bar{D}$ decay events, we exclude one charged kaon or one charged pion track and examine the variable $M^2_{{\rm miss}K{\rm or}\pi}$, defined as the difference between the missing energy squared $E^2_{\rm miss}$ and the missing momentum squared $p^2_{\rm miss}$ of the selected $D\bar{D}$ decay events. By analyzing these $M^2_{{\rm miss}K{\rm or}\pi}$ variables for both the data and the simulated cocktail vs cocktail $D\bar{D}$ process Monte Carlo events, we find the differences in efficiencies for reconstructing a charged kaon or a charged pion between the data and the Monte Carlo events as a function of the charged particle momentum. Considering the momentum distributions of the kaon and pion from these two semileptonic decays, we obtain the magnitudes of systematic differences and their uncertainties of the track

reconstruction efficiencies. The level of uncertainties in the corrections for these differences in measurements of the decay branching fractions and partial decay rates (see Sec. VI) are 0.42% and 0.28% for charged kaons and pions, respectively.

3. Uncertainty in particle identification

The differences in efficiencies for identifying a positron between the data and the Monte Carlo samples depend not only on the momentum of the positron, but also on $\cos\theta$. Considering both of these for our signal positrons, we obtain a weighted-average difference in efficiency for identifying the positron from the two semileptonic decays. After making correction for these differences in efficiencies for identifying the positrons, we obtain a systematic uncertainty of 0.16% (0.14%) on the $K^-(\pi^-)e^+\nu_e$ mode from this source.

The systematic uncertainties associated with the efficiencies for identifying a charged kaon and a charged pion are estimated using the missing mass square techniques discussed above. Taking into account the momentum distributions of the charged particles from the two semileptonic modes, we correct for the momentum-weighted efficiency differences for identifying the kaon and the pion, and we assign systematic uncertainties of 0.10% and 0.19% for charged kaons and pions, respectively.

4. Uncertainty in $E_{\gamma,\mathrm{max}}$ cut

The uncertainty associated with the $E_{\gamma,\mathrm{max}}$ requirement on the events is estimated by analyzing doubly tagged $D\bar{D}$ events with hadronic decay modes. With these events, we examine the fake photons from the EMC measurements. By analyzing these selected samples from both the data and the simulated Monte Carlo events, we find that the magnitude of difference in the number of fake photons between the data and the Monte Carlo events is 0.10%, which is set as the systematic uncertainty due to this source.

5. Uncertainty in fit to U_{miss} distribution

To estimate the systematic uncertainty in the numbers of signal events due to the fit to the U_{miss} distribution, we vary the bin size and the tail parameters of the signal function. We then repeat the fits to the U_{miss} distributions, and combine the changes in the yields in quadrature to obtain the systematic uncertainty. Since the background function is formed from many background modes with fixed relative normalizations, we also vary the relative contributions of several of the largest background modes based on the uncertainties in their branching fractions and the uncertainties in the rates of misidentifying a hadron (muon) as an electron. Finally we find that the relative sizes of this systematic uncertainty are 0.48% and 0.50% for $D^0 \to K^-e^+\nu_e$ and $D^0 \to \pi^-e^+\nu_e$, respectively.

6. Uncertainty in form factors

In order to estimate the systematic uncertainty associated with the form factor used to generate signal events in the Monte Carlo simulation, we reweight the signal Monte Carlo events so that their q^2 distributions match the measured spectra. We then remeasure the branching fraction (partial decay rates in different q^2 bins) with the new weighted efficiency (efficiency matrix). The maximum relative changes in branching fraction (partial decay rates in different q^2 bins) is 0.05%. To be conservative, we assign a relative systematic uncertainty of 0.10% to the branching fraction measurements for $D^0 \to K^-e^+\nu_e$ and $D^0 \to \pi^-e^+\nu_e$ decays.

7. Uncertainty in FSR recovery

The difference between the measured branching fraction obtained with the FSR recovery of the positron momentum and the one obtained without the FSR recovery is assigned as the most conservative systematic uncertainty due to FSR recovery. We find the magnitude of this difference to be 0.30% for both $D^0 \to K^-e^+\nu_e$ and $D^0 \to \pi^-e^+\nu_e$ decays.

8. Uncertainty due to finite Monte Carlo statistics

The uncertainties associated with the finite Monte Carlo statistics are 0.17% for both $D^0 \to K^-e^+\nu_e$ and $D^0 \to \pi^-e^+\nu_e$.

9. Uncertainty due to single tag cancelation

Most of the systematic uncertainties arising from the selection of single $\bar{D}^0$ tags are canceled due to the double tag technique. The uncanceled systematic error of MDC tracking, particle identification and π^0 selection in single tag selection is estimated by $(\sum_{\mathrm{tag}}(\epsilon'_{\mathrm{tag}}/\epsilon_{\mathrm{tag}} - 1)\times 0.25\delta_{\mathrm{tag}} \times N_{\mathrm{tag}})/(\sum_{\mathrm{tag}} N_{\mathrm{tag}})$, where ϵ'_{tag} and ϵ_{tag} are the efficiencies of reconstructing single $\bar{D}^0$ tags obtained by analyzing the Monte Carlo events of $\bar{D}^0 \to$ tag vs $D^0 \to h^-e^+\nu_e$ and $\bar{D}^0 \to$ tag vs $D^0 \to$ anything after mixing all the simulated backgrounds, respectively; N_{tag} is the number of single $\bar{D}^0$ tags reconstructed in data; δ_{tag} is the total systematic error of MDC tracking, particle identification and π^0 selection in single tag selection. Since no efficiency correction is made in the single tag selection, the uncertainty in MDC tracking (or particle identification) for charged kaon or pion is taken to be 1.0% per track, and the uncertainty in π^0 selection is taken to be 2.0% per π^0. For each single $\bar{D}^0$ tag mode, the uncertainty in MDC tracking, particle identification or π^0 selection are added linearly separately, and then they are added in quadrature to obtain the total systematic error in the single $\bar{D}^0$ tag selection. Finally, we assign a

TABLE IV. Comparison of the measured $\mathcal{B}(D^0 \to K^- e^+ \nu_e)$ and $\mathcal{B}(D^0 \to \pi^- e^+ \nu_e)$ values with those measured by other experiments and theoretical predictions based on QCD and the world-average value of τ_{D^0}.

Experiment/theory	$\mathcal{B}(D^0 \to K^- e^+ \nu_e)$ (%)	$\mathcal{B}(D^0 \to \pi^- e^+ \nu_e)$ (%)
PDG2014 [6]	3.55 ± 0.05	0.289 ± 0.008
MARK-III [21]	$3.4 \pm 0.5 \pm 0.4$	$0.39^{+0.23}_{-0.11} \pm 0.04$
CLEO [22]	$3.82 \pm 0.11 \pm 0.25$	
BES-II [17]	$3.82 \pm 0.40 \pm 0.27$	$0.33 \pm 0.13 \pm 0.03$
CLEO-c [23]	$3.50 \pm 0.03 \pm 0.04$	$0.288 \pm 0.008 \pm 0.003$
Belle [30]	$3.45 \pm 0.07 \pm 0.20$	$0.255 \pm 0.019 \pm 0.016$
BABAR [24,25]	$3.522 \pm 0.027 \pm 0.045 \pm 0.065$	$0.2770 \pm 0.0068 \pm 0.0092 \pm 0.0037$
BESIII (this work)	$3.505 \pm 0.014 \pm 0.033$	$0.295 \pm 0.004 \pm 0.003$
LQCD [26]	$3.77 \pm 0.29 \pm 0.74$	$0.316 \pm 0.025 \pm 0.070$
LQCD [27]	$2.99 \pm 0.45 \pm 0.74$	0.24 ± 0.06
QCD SR [28]	2.7 ± 0.6	
LCSR [29]	3.9 ± 1.2	0.30 ± 0.09

systematic uncertainty of 0.12% for the branching fraction measurements.

D. Comparison with other measurements

A comparison of our measured branching fractions for $D^0 \to K^- e^+ \nu_e$ and $D^0 \to \pi^- e^+ \nu_e$ decays with those previously measured by the MARK-III [21], CLEO [22], BES-II [17], CLEO [23] (at the CLEO-c experiment) and *BABAR* [24,25] collaborations as well as the world average given by the PDG [6] is given in Table IV. Our measured branching fractions for these two decays are in excellent agreement with the experimental results obtained by other experiments, but are more precise. In the Table, we also compare our branching fraction measurements to theoretical predictions for these two semileptonic decays. The precision of our measured branching fractions are much higher than those of the LQCD [26,27], the QCD sum rule [28] and the light cone sum rule (LCSR) [29] predictions.

VI. DIFFERENTIAL DECAY RATES

The differential decay rate $d\Gamma/dq^2$ for $D^0 \to K^-(\pi^-)e^+\nu_e$ is given by Eq. (1.1). The form factor $f_+^{K(\pi)}(q^2)$ can be extracted from measurements of $d\Gamma/dq^2$. Such measurements are obtained from the event rates in bins of q^2 ranging from $q_i^2 - 0.5\Delta q^2$ to $q_i^2 + 0.5\Delta q^2$, where Δq^2 is the bin width and i is the bin number.

A. Measurement of differential decay rates

The q^2 value is given by

$$q^2 = (E_e + E_\nu)^2 - (\vec{p}_e + \vec{p}_\nu)^2, \tag{6.1}$$

where E_e and $\vec{p}_e$ are the measured energy and momentum of the positron, E_ν and $\vec{p}_\nu$ are the energy and momentum of the missing neutrino:

$$E_\nu = E_{\rm miss}, \tag{6.2}$$

$$\vec{p}_\nu = E_{\rm miss}\hat{p}_{\rm miss}. \tag{6.3}$$

For the $D^0 \to K^- e^+ \nu_e$ differential rate, we divide the candidates for the decays into 18 q^2 bins. For the $D^0 \to \pi^- e^+ \nu_e$ mode, which has fewer events, we use 14 q^2 bins. The first columns of Tables V and VI give the range of each q^2 bin for $D^0 \to K^- e^+ \nu_e$ and $D^0 \to \pi^- e^+ \nu_e$, respectively.

The points with error bars in Figs. 4 and 5 show the $U_{\rm miss}$ distributions for the $D^0 \to K^- e^+ \nu_e$ and $D^0 \to \pi^- e^+ \nu_e$ decays for each q^2 bin, respectively. Fits to these distributions that follow the procedure described in Sec. IV C

TABLE V. Summary of the range of each q^2 bin, the number of the observed events $N_{\rm observed}$, the number of produced events $N_{\rm produced}$, and the partial decay rate $\Delta\Gamma$ in each q^2 bin for $D^0 \to K^- e^+ \nu_e$ decays.

$q^2(\mathrm{GeV}^2/\mathrm{c}^4)$	$N_{\rm observed}$	$N_{\rm produced}$	$\Delta\Gamma(\mathrm{ns}^{-1})$
(0.0, 0.1)	7876.1 ± 94.2	10094.9 ± 132.3	8.812 ± 0.116
(0.1, 0.2)	7504.3 ± 90.5	10015.4 ± 140.8	8.743 ± 0.123
(0.2, 0.3)	6940.5 ± 87.2	9502.6 ± 142.0	8.295 ± 0.124
(0.3, 0.4)	6376.0 ± 83.4	8667.9 ± 138.6	7.567 ± 0.121
(0.4, 0.5)	6139.8 ± 81.9	8575.9 ± 137.7	7.486 ± 0.120
(0.5, 0.6)	5460.5 ± 77.1	7384.0 ± 128.1	6.446 ± 0.112
(0.6, 0.7)	5120.3 ± 74.7	7101.8 ± 125.8	6.200 ± 0.110
(0.7, 0.8)	4545.5 ± 70.5	6322.2 ± 120.2	5.519 ± 0.105
(0.8, 0.9)	4159.4 ± 67.1	5760.3 ± 113.3	5.028 ± 0.099
(0.9, 1.0)	3680.7 ± 63.2	5183.5 ± 107.6	4.525 ± 0.094
(1.0, 1.1)	3199.6 ± 58.9	4550.0 ± 100.2	3.972 ± 0.087
(1.1, 1.2)	2637.1 ± 53.5	3810.2 ± 92.4	3.326 ± 0.081
(1.2, 1.3)	2239.1 ± 49.4	3239.1 ± 84.3	2.828 ± 0.074
(1.3, 1.4)	1752.1 ± 43.9	2621.2 ± 77.3	2.288 ± 0.067
(1.4, 1.5)	1301.0 ± 37.7	1989.4 ± 67.4	1.737 ± 0.059
(1.5, 1.6)	927.5 ± 32.0	1505.1 ± 59.0	1.314 ± 0.052
(1.6, 1.7)	541.3 ± 24.6	983.4 ± 50.3	0.858 ± 0.044
(1.7, $q^2_{\rm max}$)	188.2 ± 15.1	434.2 ± 39.6	0.379 ± 0.035

TABLE VI. Summary of the range of each q^2 bin, the number of the observed events $N_{\rm observed}$, the number of produced events $N_{\rm produced}$, and the partial decay rate $\Delta\Gamma$ in each q^2 bin for $D^0 \to \pi^- e^+ \nu_e$ decays.

$q^2(\mathrm{GeV}^2/\mathrm{c}^4)$	$N_{\rm observed}$	$N_{\rm produced}$	$\Delta\Gamma(\mathrm{ns}^{-1})$
(0.0, 0.2)	814.4 ± 30.9	1066.9 ± 43.2	0.931 ± 0.038
(0.2, 0.4)	697.2 ± 28.7	935.1 ± 42.8	0.816 ± 0.037
(0.4, 0.6)	634.6 ± 27.7	836.6 ± 41.3	0.730 ± 0.036
(0.6, 0.8)	654.6 ± 27.8	850.1 ± 40.6	0.742 ± 0.035
(0.8, 1.0)	643.2 ± 27.3	840.2 ± 39.9	0.733 ± 0.035
(1.0, 1.2)	578.6 ± 26.3	744.6 ± 37.7	0.650 ± 0.033
(1.2, 1.4)	509.9 ± 24.7	651.1 ± 35.1	0.568 ± 0.031
(1.4, 1.6)	438.6 ± 23.2	551.6 ± 32.8	0.481 ± 0.029
(1.6, 1.8)	412.6 ± 22.3	534.7 ± 31.7	0.467 ± 0.028
(1.8, 2.0)	320.9 ± 19.8	420.6 ± 28.6	0.367 ± 0.025
(2.0, 2.2)	245.8 ± 17.0	324.0 ± 24.7	0.283 ± 0.022
(2.2, 2.4)	165.4 ± 14.1	229.9 ± 21.7	0.201 ± 0.019
(2.4, 2.6)	93.6 ± 10.7	129.2 ± 16.7	0.113 ± 0.015
(2.6, $q^2_{\rm max}$)	75.8 ± 10.0	107.2 ± 15.0	0.094 ± 0.013

give the signal yields $N_{\rm observed}$ for each q^2 bin. In these figures, the blue solid lines show the best fit to the data, while the red dashed lines show the background. In these fits, the background normalizations are left free.

To account for detection efficiency and detector resolution, the number of events $N^i_{\rm observed}$ observed in the ith q^2 bin is extracted from the relation

$$N^i_{\rm observed} = \sum_{j=1}^{N_{\rm bins}} \epsilon_{ij} N^j_{\rm produced}, \tag{6.4}$$

where ϵ_{ij} is the overall efficiency matrix that describes the efficiency and migration across q^2 bins.

The efficiency matrix element ϵ_{ij} is obtained by

$$\epsilon_{ij} = \frac{N^{\rm reconstructed}_{ij}}{N^{\rm generated}_{j}} \frac{1}{\epsilon_{\rm tag}} f^{\rm trk+PID}_{{\rm corr},ij}, \tag{6.5}$$

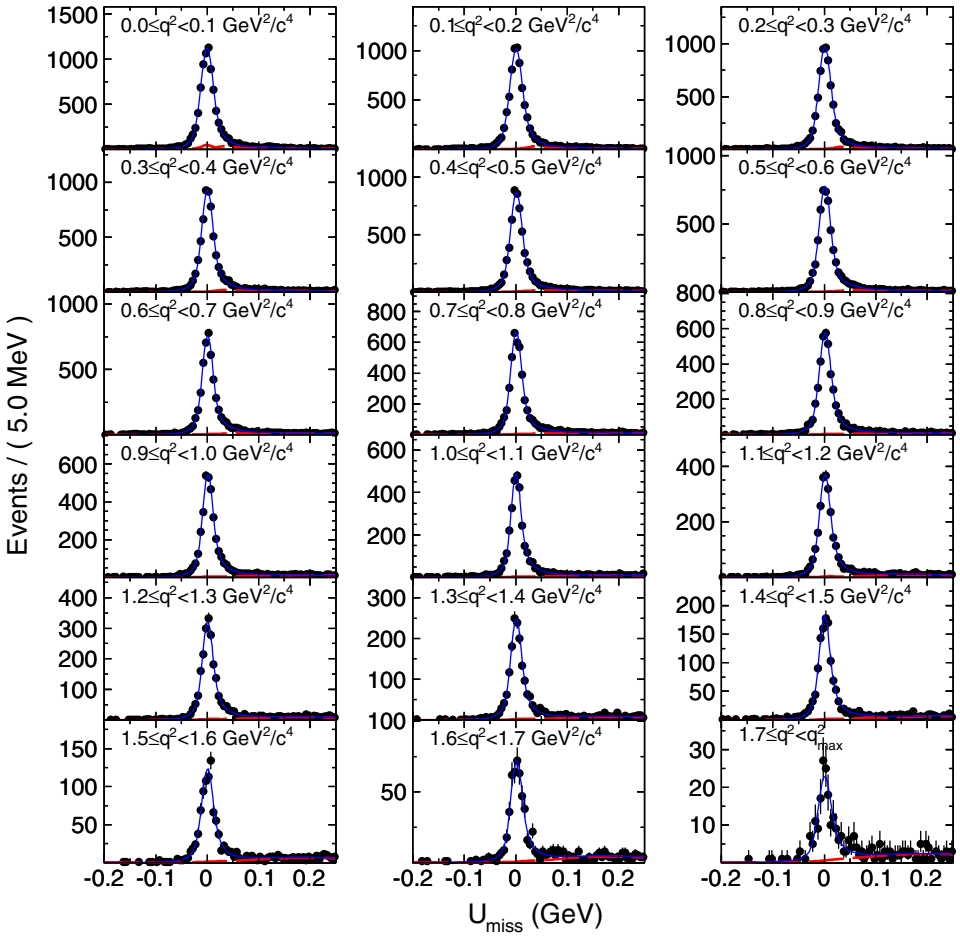

FIG. 4 (color online). Distributions of $U_{\rm miss}$ for $\bar{D}^0$ tags vs $D^0 \to K^- e^+ \nu_e$ with the squared four-momentum transfer q^2 filled in different q^2 bins. The dots with error bars show the data, the blue solid lines show the best fits to the data, while the red dashed lines show the background shapes.

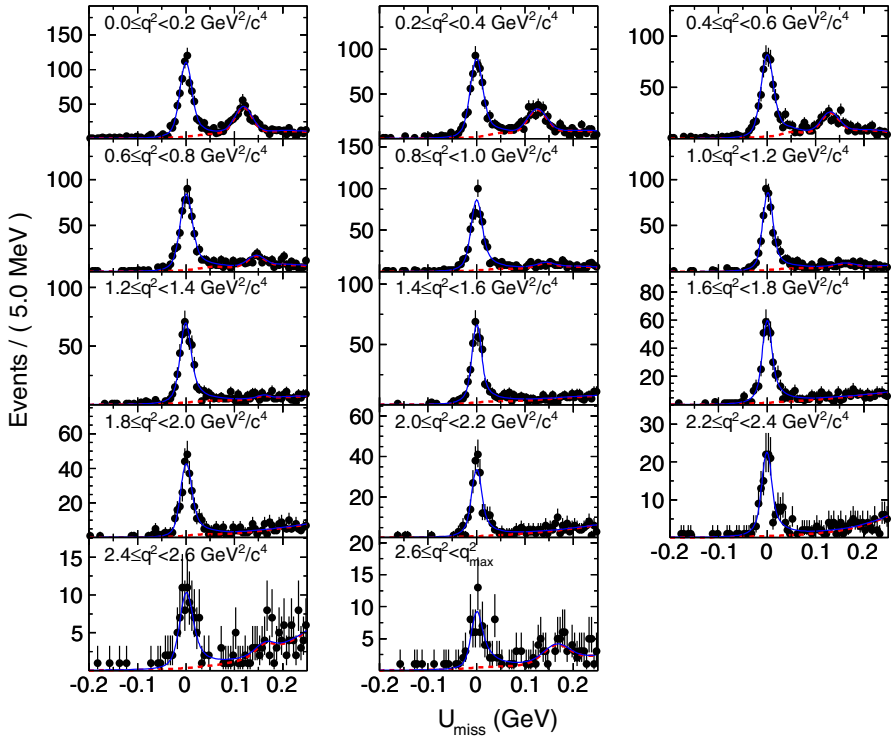

FIG. 5 (color online). Distributions of $U_{\rm miss}$ for $\bar{D}^0$ tags vs $D^0 \to \pi^- e^+ \nu_e$ with the squared four-momentum transfer q^2 filled in different q^2 bins. The dots with error bars show the data, the blue solid lines show the best fits to the data, while the red dashed lines show the background shapes.

where $N_{ij}^{\rm reconstructed}$ is the number of signal Monte Carlo events generated in the jth q^2 bin and reconstructed in the ith q^2 bin, $N_j^{\rm generated}$ is the total number of the signal Monte Carlo events which are generated in the jth q^2 bin, $\epsilon_{\rm tag}$ is the single $\bar{D}^0$ tag efficiency, and $f_{{\rm corr},ij}^{\rm trk+PID}$ is the efficiency correction matrix for correcting the Monte Carlo deviations for tracking and particle identification efficiencies of each element of the efficiency matrix described above.

Table VII presents the average overall efficiency matrix for the $D^0 \to K^- e^+ \nu_e$ mode. To produce this average

TABLE VII. Weighted efficiency matrix ϵ_{ij} (in percent) for $D^0 \to K^- e^+ \nu_e$. The column gives the true q^2 bin j, while the row gives the reconstructed q^2 bin i.

ϵ_{ij}	1	2	3	4	5	6	7	8	9	10	11	12	13	14	15	16	17	18
1	71.62	5.39	0.70	0.31	0.11	0.03	0.01	0.00	0.01	0.00	0.00	0.00	0.00	0.00	0.00	0.00	0.00	0.00
2	2.54	65.14	6.31	0.86	0.42	0.15	0.02	0.01	0.01	0.00	0.00	0.00	0.00	0.00	0.00	0.00	0.00	0.00
3	0.05	3.19	62.49	6.53	0.84	0.37	0.10	0.05	0.01	0.02	0.00	0.00	0.00	0.01	0.00	0.02	0.00	0.00
4	0.02	0.09	3.61	61.47	7.07	0.79	0.31	0.09	0.01	0.00	0.01	0.01	0.00	0.00	0.00	0.00	0.00	0.00
5	0.01	0.02	0.11	3.64	60.77	6.93	0.88	0.29	0.08	0.01	0.01	0.03	0.00	0.00	0.00	0.00	0.00	0.00
6	0.00	0.03	0.05	0.10	3.98	61.58	6.81	0.80	0.27	0.08	0.01	0.03	0.00	0.00	0.01	0.00	0.00	0.00
7	0.01	0.01	0.01	0.05	0.14	4.16	60.75	6.71	0.66	0.27	0.04	0.02	0.02	0.00	0.00	0.00	0.00	0.00
8	0.00	0.00	0.02	0.01	0.05	0.16	4.12	60.04	6.70	0.75	0.22	0.04	0.04	0.02	0.00	0.00	0.00	0.00
9	0.00	0.00	0.01	0.03	0.01	0.05	0.18	4.12	60.61	6.64	0.75	0.17	0.03	0.03	0.01	0.00	0.00	0.00
10	0.00	0.01	0.00	0.00	0.02	0.05	0.05	0.17	4.01	59.99	6.38	0.62	0.12	0.04	0.03	0.00	0.00	0.00
11	0.00	0.00	0.01	0.00	0.01	0.01	0.04	0.09	0.20	3.91	59.97	5.84	0.62	0.10	0.01	0.02	0.00	0.00
12	0.00	0.00	0.00	0.00	0.00	0.01	0.02	0.03	0.05	0.15	3.90	59.02	5.61	0.46	0.09	0.04	0.00	0.00
13	0.00	0.00	0.00	0.00	0.00	0.00	0.00	0.00	0.03	0.12	0.20	3.82	59.59	5.15	0.47	0.11	0.03	0.00
14	0.00	0.00	0.00	0.00	0.00	0.00	0.00	0.00	0.02	0.03	0.10	0.23	3.63	57.71	5.06	0.34	0.00	0.00
15	0.00	0.00	0.00	0.00	0.00	0.00	0.00	0.00	0.01	0.01	0.03	0.07	0.18	3.47	56.72	4.57	0.17	0.05
16	0.00	0.00	0.00	0.00	0.00	0.00	0.00	0.00	0.00	0.01	0.00	0.02	0.03	0.28	2.82	54.82	3.66	0.17
17	0.00	0.00	0.00	0.00	0.00	0.00	0.00	0.01	0.00	0.00	0.01	0.00	0.02	0.04	0.21	2.66	49.34	2.10
18	0.00	0.01	0.00	0.00	0.00	0.00	0.00	0.00	0.00	0.00	0.00	0.00	0.01	0.01	0.02	0.05	1.95	38.30

overall efficiency matrix, we combine the efficiency matrices for each tag mode weighted by its yields shown in Table I. The diagonal elements of the matrix give the overall efficiency for $D^0 \to K^- e^+ \nu_e$ decays to be reconstructed in the correct q^2 bin in the recoil of the single $\bar{D}^0$ tags, while the neighboring off-diagonal elements of the matrix give the overall efficiency for cross feed between different q^2 bins. Similarly, Table VIII presents the average overall efficiency matrix for the $D^0 \to \pi^- e^+ \nu_e$ channel.

The number of $D^0 \to K^-(\pi^-)e^+\nu_e$ semileptonic decay events produced with q^2 filled in the ith q^2 bin is obtained from

$$N^i_{\rm produced} = \sum_j^{N_{\rm bins}} (\epsilon^{-1})_{ij} N^j_{\rm observed}, \tag{6.6}$$

with a statistical error given by

$$\sigma_{\rm stat}(N^i_{\rm produced}) = \sqrt{\sum_j^{N_{\rm bins}} (\epsilon^{-1})^2_{ij} (\sigma_{\rm stat}(N^j_{\rm observed}))^2}, \tag{6.7}$$

in which $\sigma_{\rm stat}(N^j_{\rm observed})$ is the statistical error of $N^j_{\rm observed}$. The partial width for the ith bin is given by

$$\Delta\Gamma_i = \frac{N^i_{\rm produced}}{\tau_{D^0} N_{\rm tag}}, \tag{6.8}$$

where τ_{D^0} is the lifetime of the D^0 meson and $N_{\rm tag}$ is the number of the single $\bar{D}^0$ tags.

The numbers of the signal events and q^2-dependent partial widths for $D^0 \to K^- e^+ \nu_e$ and $D^0 \to \pi^- e^+ \nu_e$ are summarized in Tables V and VI, respectively, where the uncertainties are statistical only.

B. Fitting partial decay rates to extract form factors

To extract the form-factor parameters, we fit the theoretical predictions of the rates to the measured partial decay rates. Taking into account the correlations of the measured partial decay rates among q^2 bins, the χ^2 to be minimized is defined as

$$\chi^2 = \sum_{i,j=1}^{N_{\rm bins}} (\Delta\Gamma_i^{\rm measured} - \Delta\Gamma_i^{\rm expected}) \times C^{-1}_{ij} (\Delta\Gamma_j^{\rm measured} - \Delta\Gamma_j^{\rm expected}), \tag{6.9}$$

where $\Delta\Gamma_i^{\rm measured}$ is the measured partial decay rate in q^2 bin i, C^{-1}_{ij} is the inverse of the covariance matrix C_{ij} which accounts for the correlations between the measured partial decay rates in different q^2 bins, and $N_{\rm bins}$ is the number of q^2 bins. The expected partial decay rate in the ith q^2 bin is given by

$$\Delta\Gamma_i^{\rm expected} = \int_{q^2_{\min(i)}}^{q^2_{\max(i)}} \frac{G_F^2 |V_{cs(d)}|^2}{24\pi^3} |\vec{p}_{K(\pi)}|^3 |f_+^{K(\pi)}(q^2)|^2 dq^2, \tag{6.10}$$

where $q^2_{\min(i)}$ and $q^2_{\max(i)}$ are the lower and higher boundaries of the q^2 bin i, respectively. In the fits, all parameters of the form-factor parametrizations are left free.

We separate the covariance matrix into two parts, one is the statistical covariance matrix $C^{\rm stat}_{ij}$ and the other is the systematic covariance matrix $C^{\rm sys}_{ij}$. The statistical covariance matrix is determined by

$$C^{\rm stat}_{ij} = \left(\frac{1}{\tau_{D^0} N_{\rm tag}}\right)^2 \sum_\alpha \epsilon^{-1}_{i\alpha} \epsilon^{-1}_{j\alpha} (\sigma(N^\alpha_{\rm observed}))^2. \tag{6.11}$$

TABLE VIII. Weighted efficiency matrix ϵ_{ij} (in percent) for $D^0 \to \pi^- e^+ \nu_e$. The column gives the true q^2 bin j, while the row gives the reconstructed q^2 bin i.

ϵ_{ij}	1	2	3	4	5	6	7	8	9	10	11	12	13	14
1	71.86	4.55	0.57	0.04	0.01	0.00	0.00	0.00	0.00	0.00	0.00	0.00	0.00	0.00
2	1.71	67.50	5.18	0.47	0.03	0.01	0.00	0.00	0.00	0.00	0.01	0.00	0.00	0.03
3	0.05	2.11	67.78	5.22	0.32	0.03	0.00	0.01	0.00	0.00	0.00	0.00	0.00	0.00
4	0.02	0.07	2.42	69.05	5.30	0.25	0.01	0.00	0.00	0.00	0.00	0.00	0.01	0.00
5	0.00	0.03	0.10	2.64	69.00	5.11	0.26	0.02	0.01	0.00	0.00	0.00	0.00	0.00
6	0.01	0.02	0.03	0.14	2.57	70.20	4.85	0.17	0.02	0.00	0.00	0.00	0.00	0.00
7	0.01	0.02	0.04	0.05	0.15	2.67	71.01	4.46	0.13	0.01	0.00	0.00	0.00	0.00
8	0.01	0.02	0.02	0.04	0.10	0.23	2.75	71.32	4.38	0.11	0.00	0.00	0.00	0.00
9	0.01	0.01	0.01	0.03	0.04	0.12	0.26	2.70	70.75	3.73	0.08	0.01	0.00	0.00
10	0.00	0.00	0.00	0.00	0.03	0.06	0.16	0.29	2.55	69.48	3.50	0.14	0.02	0.00
11	0.00	0.00	0.00	0.00	0.00	0.02	0.07	0.12	0.32	2.72	69.08	3.28	0.03	0.02
12	0.00	0.00	0.00	0.00	0.00	0.00	0.01	0.05	0.19	0.38	2.63	65.19	3.09	0.01
13	0.00	0.00	0.00	0.00	0.01	0.00	0.00	0.01	0.01	0.13	0.41	2.49	64.07	2.81
14	0.00	0.00	0.00	0.00	0.00	0.00	0.01	0.00	0.01	0.02	0.08	0.33	2.29	66.78

TABLE IX. Statistical correlation matrix and relative statistical uncertainty of the measured partial decay rate in each q^2 bin for $D^0 \to K^- e^+ \nu_e$.

q^2 bin	1	2	3	4	5	6	7	8	9	10
Correlation ρ_{ij}	1.000									
	−0.115	1.000								
	0.003	−0.146	1.000							
	−0.003	0.005	−0.159	1.000						
	−0.001	−0.005	0.007	−0.171	1.000					
	0.000	−0.001	−0.005	0.011	−0.172	1.000				
	0.000	0.000	0.000	−0.004	0.009	−0.175	1.000			
	0.000	0.000	−0.001	0.000	−0.004	0.010	−0.174	1.000		
	0.000	0.000	0.000	0.000	0.000	−0.004	0.011	−0.174	1.000	
	0.000	0.000	0.000	0.000	0.000	−0.001	−0.004	0.010	−0.171	1.000
	0.000	0.000	0.000	0.000	0.000	0.000	0.000	−0.003	0.008	−0.166
	0.000	0.000	0.000	0.000	0.000	0.000	0.000	0.000	−0.002	0.010
	0.000	0.000	0.000	0.000	0.000	0.000	0.000	0.000	0.000	−0.003
	0.000	0.000	0.000	0.000	0.000	0.000	0.000	0.000	−0.001	0.000
	0.000	0.000	0.000	0.000	0.000	0.000	0.000	0.000	0.000	0.000
	0.000	0.000	0.000	0.000	0.000	0.000	0.000	0.000	0.000	0.000
	0.000	0.000	0.000	0.000	0.000	0.000	0.000	0.000	0.000	0.000
	0.000	−0.001	0.000	0.000	0.000	0.000	0.000	0.000	0.000	0.000
Statistical uncertainty	1.31%	1.41%	1.49%	1.60%	1.61%	1.74%	1.77%	1.90%	1.97%	2.08%
q^2 bin	11	12	13	14	15	16	17	18		
Correlation ρ_{ij}	1.000									
	−0.159	1.000								
	0.007	−0.154	1.000							
	−0.002	0.007	−0.146	1.000						
	0.000	−0.002	0.006	−0.145	1.000					
	0.000	−0.001	−0.001	0.003	−0.127	1.000				
	0.000	0.000	−0.001	0.000	0.004	−0.119	1.000			
	0.000	0.000	0.000	0.000	−0.001	0.006	−0.098	1.000		
Statistical uncertainty	2.20%	2.42%	2.60%	2.95%	3.39%	3.92%	5.11%	9.12%		

Tables IX and X give the statistical correlation matrix and relative statistical uncertainties of the measured partial decay rates for $D^0 \to K^- e^+ \nu_e$ and $D^0 \to \pi^- e^+ \nu_e$ decays, respectively.

Inserting the inverse statistical covariance matrix $(C^{\rm stat})^{-1}$ into Eq. (6.9), replacing the form factor $f_+^{K(\pi)}(q^2)$ in Eq. (6.10) with different form-factor parametrizations discussed in the Sec. II, and fitting to the measured partial decay rates yields the product of $f_+^{K(\pi)}(0)$ and $|V_{cs(d)}|$ as well as the parameters of the form factor.

C. Systematic uncertainties in form factor measurements

1. Systematic covariance matrix

For each source of systematic uncertainty, an $N_{\rm bins} \times N_{\rm bins}$ covariance matrix is estimated. The total systematic covariance matrix is obtained by summing all these matrices.

(1) *Number of $\bar{D}^0$ tags*.—The uncertainties associated with the number of the single $\bar{D}^0$ tags are fully correlated across all q^2 bins. The systematic covariance contributed from the uncertainty in the number of single $\bar{D}^0$ tags is calculated by

$$C_{ij}^{\rm sys}(N_{\rm tag}) = \Delta\Gamma_i \Delta\Gamma_j \left(\frac{\sigma(N_{\rm tag})}{N_{\rm tag}}\right)^2, \qquad (6.12)$$

where $\sigma(N_{\rm tag})/N_{\rm tag}$ is the relative uncertainty of the number of the single $\bar{D}^0$ tags.

(2) *D^0 lifetime*.—The uncertainty associated with the lifetime of the D^0 meson are fully correlated across all q^2 bins, so the systematic covariance is calculated by

$$C_{ij}^{\rm sys}(\tau_{D^0}) = \Delta\Gamma_i \Delta\Gamma_j \left(\frac{\sigma(\tau_{D^0})}{\tau_{D^0}}\right)^2, \qquad (6.13)$$

where $\sigma(\tau_{D^0})$ is the uncertainty of the D^0 lifetime taken from PDG [6].

(3) *Monte Carlo statistics*.—The systematic uncertainties and correlations in q^2 bins due to the limited size of the Monte Carlo samples used to determine the efficiency matrices are calculated by

TABLE X. Statistical correlation matrix and relative statistical uncertainty of the measured partial decay rate in each q^2 bin for $D^0 \to \pi^- e^+ \nu_e$.

q^2 bin	1	2	3	4	5	6	7	8	9	10
Correlation ρ_{ij}	1.000									
	−0.087	1.000								
	−0.001	−0.105	1.000							
	0.000	0.002	−0.110	1.000						
	0.000	0.000	0.004	−0.114	1.000					
	0.000	0.000	−0.001	0.004	−0.108	1.000				
	0.000	0.000	0.000	−0.001	0.003	−0.104	1.000			
	0.000	0.000	0.000	0.000	−0.001	0.003	−0.099	1.000		
	0.000	0.000	0.000	0.000	0.000	−0.002	0.002	−0.098	1.000	
	0.000	0.000	0.000	0.000	0.000	−0.001	−0.002	0.001	−0.087	1.000
	0.000	0.000	0.000	0.000	0.000	0.000	−0.001	−0.002	0.000	−0.088
	0.000	0.000	0.000	0.000	0.000	0.000	0.000	−0.001	−0.004	−0.003
	0.000	0.000	0.000	0.000	0.000	0.000	0.000	0.000	0.000	−0.003
	0.000	0.000	0.000	0.000	0.000	0.000	0.000	0.000	0.000	0.000
Statistical uncertainty	4.05%	4.58%	4.93%	4.77%	4.75%	5.07%	5.39%	5.94%	5.93%	6.80%
q^2 bin	11	12	13	14						
Correlation ρ_{ij}	1.000									
	−0.087	1.000								
	−0.003	−0.086	1.000							
	−0.001	−0.002	−0.077	1.000						
Statistical uncertainty	7.64%	9.45%	12.96%	13.95%						

$$C_{ij}^{\rm sys}({\rm MC\,stat}) = \left(\frac{1}{\tau_{D^0} N_{\rm tag}}\right)^2 \sum_{\alpha\beta} (N^{\alpha}_{\rm observed} \times N^{\beta}_{\rm observed} {\rm Cov}(\epsilon^{-1}_{i\alpha}, \epsilon^{-1}_{j\beta})), \quad (6.14)$$

where the covariance of the inverse efficiency matrix elements are given by [31]

$${\rm Cov}(\epsilon^{-1}_{\alpha\beta}, \epsilon^{-1}_{ab}) = \sum_{ij} (\epsilon^{-1}_{\alpha i} \epsilon^{-1}_{ai})[\sigma^2(\epsilon_{ij})]^2 (\epsilon^{-1}_{j\beta} \epsilon^{-1}_{jb}). \quad (6.15)$$

(4) *Form factor structure*.—In order to estimate the systematic uncertainty associated with the form factor used to generate signal events in the Monte Carlo simulation, we reweight the signal Monte Carlo events so that the q^2 spectra agree with the measured spectra. We then recalculate the partial decay rates with the new efficiency matrices which are determined using the weighted Monte Carlo events. The covariance matrix due to this source is assigned via

$$C_{ij}^{\rm sys}({\rm F.F.}) = \delta(\Delta\Gamma_i)\delta(\Delta\Gamma_j), \quad (6.16)$$

where $\delta(\Delta\Gamma_i)$ denotes the change in the measured partial rate in the ith q^2 bin.

(5) $E_{\gamma,\rm max}$ *cut*.—We assign systematic uncertainties of 0.10% due to the $E_{\gamma,\rm max}$ requirement on the selected events in each q^2 bin, and assume that they are fully correlated between q^2 bins. The systematic covariance due to this requirement can be obtained by

$$C_{ij}^{\rm sys}(E_{\gamma,\rm max}) = \sigma(\Delta\Gamma_i)\sigma(\Delta\Gamma_j), \quad (6.17)$$

where $\sigma(\Delta\Gamma_i) = 0.10\% \times \Delta\Gamma_i$.

(6) $U_{\rm miss}$ *fits*.—The technique of fitting $U_{\rm miss}$ distributions affects the numbers of signal events observed in q^2 bins. The covariance matrix due to the $U_{\rm miss}$ fits is determined by

$$C_{ij}^{\rm sys}(U_{\rm miss}{\rm Fit}) = \left(\frac{1}{\tau_D N_{\rm tag}}\right)^2 \times \sum_{\alpha} \epsilon^{-1}_{i\alpha} \epsilon^{-1}_{j\alpha} (\sigma^{\rm Fit}_{\alpha})^2, \quad (6.18)$$

where $\sigma^{\rm Fit}_{\alpha}$ is the systematic uncertainty of the number of the signal events observed in the bin α due to fitting $U_{\rm miss}$ distribution, evaluated as described in Sec. V C 5.

(7) *Tracking and PID efficiencies*.—The covariance matrices for the systematic uncertainties associated with the tracking efficiencies and the particle identification efficiencies for the charged particles are obtained in the following way. We first vary the correction coefficients for tracking (PID) efficiencies by $\pm 1\sigma$, then remeasure the partial decay rates using the efficiency matrices obtained from the recorrected

TABLE XI. Systematic correlation matrix and relative systematic uncertainty of the measured partial decay rate in each q^2 bin for $D^0 \to K^- e^+ \nu_e$.

q^2 bin	1	2	3	4	5	6	7	8	9	10
Correlation ρ_{ij}	1.000									
	0.284	1.000								
	0.356	0.407	1.000							
	0.350	0.482	0.406	1.000						
	0.354	0.481	0.496	0.412	1.000					
	0.350	0.477	0.485	0.499	0.419	1.000				
	0.353	0.481	0.492	0.496	0.513	0.419	1.000			
	0.350	0.477	0.488	0.496	0.506	0.509	0.426	1.000		
	0.340	0.465	0.477	0.485	0.498	0.493	0.506	0.414	1.000	
	0.332	0.454	0.464	0.472	0.482	0.479	0.483	0.489	0.388	1.000
	0.317	0.433	0.442	0.449	0.457	0.455	0.461	0.458	0.456	0.345
	0.297	0.406	0.414	0.419	0.428	0.425	0.429	0.428	0.419	0.413
	0.282	0.386	0.395	0.400	0.409	0.407	0.411	0.410	0.404	0.390
	0.264	0.361	0.370	0.377	0.386	0.384	0.388	0.388	0.381	0.369
	0.222	0.304	0.312	0.317	0.325	0.323	0.326	0.326	0.321	0.310
	0.211	0.288	0.297	0.303	0.312	0.310	0.314	0.315	0.310	0.299
	0.170	0.233	0.241	0.248	0.256	0.255	0.259	0.259	0.257	0.247
	0.120	0.163	0.172	0.180	0.188	0.187	0.191	0.192	0.192	0.183
Systematic uncertainty	1.67%	1.21%	1.20%	1.24%	1.23%	1.24%	1.25%	1.25%	1.30%	1.32%
q^2 bin	11	12	13	14	15	16	17	18		
Correlation ρ_{ij}	1.000									
	0.291	1.000								
	0.377	0.246	1.000							
	0.349	0.331	0.214	1.000						
	0.295	0.273	0.268	0.140	1.000					
	0.283	0.263	0.253	0.243	0.101	1.000				
	0.233	0.216	0.208	0.197	0.170	0.063	1.000			
	0.171	0.157	0.152	0.146	0.122	0.127	0.019	1.000		
Systematic uncertainty	1.36%	1.42%	1.50%	1.62%	1.93%	2.04%	2.78%	4.66%		

signal Monte Carlo events. The covariance matrix due to this source is assigned via

$$C_{ij}^{\rm sys}({\rm Tracking, PID}) = \delta(\Delta\Gamma_i)\delta(\Delta\Gamma_j), \quad (6.19)$$

where $\delta(\Delta\Gamma_i)$ denotes the change in the measured partial decay rate in the ith q^2 bin.

(8) *FSR recovery.*—To estimate the systematic covariance matrix associated with the FSR recovery of the positron momentum, we remeasure the partial decay rates without the FSR recovery. The covariance matrix due to this source is assigned via

$$C_{ij}^{\rm sys}({\rm FSR}) = \delta(\Delta\Gamma_i)\delta(\Delta\Gamma_j), \quad (6.20)$$

where $\delta(\Delta\Gamma_i)$ denotes the change in the measured partial decay rate in ith q^2 bin.

(9) *Single tag cancelation.*—We take the systematic uncertainties associated with single tag cancellation as 0.12% in each q^2 bin, and assume they are fully correlated between different q^2 bins.

The total systematic correlation matrix and relative systematic uncertainties for measurements of the partial decay rates of the two semileptonic decays of $D^0 \to K^- e^+ \nu_e$ and $D^0 \to \pi^- e^+ \nu_e$ are presented in the Tables XI and XII, respectively.

2. Systematic uncertainty in measurements of form factor parameters

To obtain the systematic uncertainty of the parameters of the form factors obtained from the fits, we add the matrix elements of the statistical covariance matrix and systematic covariance matrix together. We then repeat the fits to the partial decay rates.

The central values of the form factor parameters are taken from the results obtained by fitting the data with the combined statistical and systematic covariance matrix together. The quadrature difference between the uncertainties of the fit parameters obtained from the fits with the combined covariance matrix and the uncertainties of the fit parameters obtained from the fits with only the statistical covariance matrix is taken as the systematic error of the measured form factor parameter.

TABLE XII. Systematic correlation matrix and relative systematic uncertainty of the measured partial decay rate in each q^2 bin for $D^0 \to \pi^- e^+ \nu_e$.

q^2 bin	1	2	3	4	5	6	7	8	9	10
Correlation ρ_{ij}	1.000									
	0.271	1.000								
	0.286	0.200	1.000							
	0.305	0.299	0.183	1.000						
	0.252	0.246	0.220	0.137	1.000					
	0.276	0.272	0.240	0.263	0.134	1.000				
	0.200	0.197	0.174	0.187	0.158	0.077	1.000			
	0.206	0.207	0.183	0.197	0.163	0.187	0.048	1.000		
	0.174	0.176	0.156	0.168	0.140	0.155	0.115	0.031	1.000	
	0.201	0.205	0.181	0.195	0.162	0.182	0.129	0.143	0.043	1.000
	0.169	0.173	0.153	0.165	0.138	0.154	0.111	0.119	0.101	0.043
	0.132	0.135	0.120	0.129	0.108	0.121	0.088	0.094	0.077	0.093
	0.144	0.147	0.130	0.141	0.117	0.133	0.096	0.103	0.089	0.101
	0.110	0.107	0.093	0.102	0.086	0.097	0.069	0.074	0.063	0.074
Systematic uncertainty	1.58%	1.47%	1.65%	1.53%	1.85%	1.66%	2.28%	2.09%	2.42%	2.10%
q^2 bin	11	12	13	14						
Correlation ρ_{ij}	1.000									
	0.002	1.000								
	0.083	−0.020	1.000							
	0.062	0.047	−0.023	1.000						
Systematic uncertainty	2.43%	3.09%	2.98%	4.92%						

D. Results of form-factor measurements

After considering the effects of the systematic uncertainties on the fitted parameters, we finally obtain the results of these fits to the partial decay rates with each form-factor model. The results of these fits are summarized in Table XIII, where the first errors are statistical and the second systematic. The fits to the differential decay rates for $D^0 \to K^- e^+ \nu_e$ and $D^0 \to \pi^- e^+ \nu_e$ are shown in Figs. 6 and 7, respectively.

Figures 8 and 9 show the projections of fits onto $f_+(q^2)$ for the $D^0 \to K^- e^+ \nu_e$ and $D^0 \to \pi^- e^+ \nu_e$ decays, respectively. In these two figures, the dots with error bars show the measured values of the form factors, $f_+^{K(\pi)}(q^2)$, which are obtained with

$$f_+^{K(\pi)}(q_i^2) = \sqrt{\frac{\Delta\Gamma_i}{\Delta q_i^2} \frac{24\pi^3}{G_F^2 p'^3_{K(\pi)} |V_{cs(d)}|^2}} \tag{6.21}$$

TABLE XIII. Summary of results of form factor fits to the data.

		Single pole model		
Decay mode	$f_+^{K(\pi)}(0)\lvert V_{cs(d)}\rvert$	$M_{\rm pole}(\mathrm{GeV}/c^2)$		χ^2/d.o.f.
$D^0 \to K^- e^+ \nu_e$	$0.7209 \pm 0.0022 \pm 0.0035$	$1.921 \pm 0.010 \pm 0.007$		18.8/16
$D^0 \to \pi^- e^+ \nu_e$	$0.1475 \pm 0.0014 \pm 0.0005$	$1.911 \pm 0.012 \pm 0.004$		20.0/12
		Modified pole model		
Decay mode	$f_+^{K(\pi)}(0)\lvert V_{cs(d)}\rvert$	α		χ^2/d.o.f.
$D^0 \to K^- e^+ \nu_e$	$0.7163 \pm 0.0024 \pm 0.0034$	$0.309 \pm 0.020 \pm 0.013$		20.2/16
$D^0 \to \pi^- e^+ \nu_e$	$0.1437 \pm 0.0017 \pm 0.0008$	$0.279 \pm 0.035 \pm 0.011$		12.6/12
		Two-parameter series expansion		
Decay mode	$f_+^{K(\pi)}(0)\lvert V_{cs(d)}\rvert$	r_1		χ^2/d.o.f.
$D^0 \to K^- e^+ \nu_e$	$0.7172 \pm 0.0025 \pm 0.0035$	$-2.2286 \pm 0.0864 \pm 0.0573$		19.6/16
$D^0 \to \pi^- e^+ \nu_e$	$0.1435 \pm 0.0018 \pm 0.0009$	$-2.0365 \pm 0.0807 \pm 0.0257$		12.8/12
		Three-parameter series expansion		
Decay mode	$f_+^{K(\pi)}(0)\lvert V_{cs(d)}\rvert$	r_1	r_2	χ^2/d.o.f.
$D^0 \to K^- e^+ \nu_e$	$0.7195 \pm 0.0035 \pm 0.0041$	$-2.3338 \pm 0.1587 \pm 0.0804$	$3.4188 \pm 3.9090 \pm 2.4098$	19.1/15
$D^0 \to \pi^- e^+ \nu_e$	$0.1420 \pm 0.0024 \pm 0.0010$	$-1.8432 \pm 0.2212 \pm 0.0690$	$-1.3874 \pm 1.4615 \pm 0.4680$	11.9/11

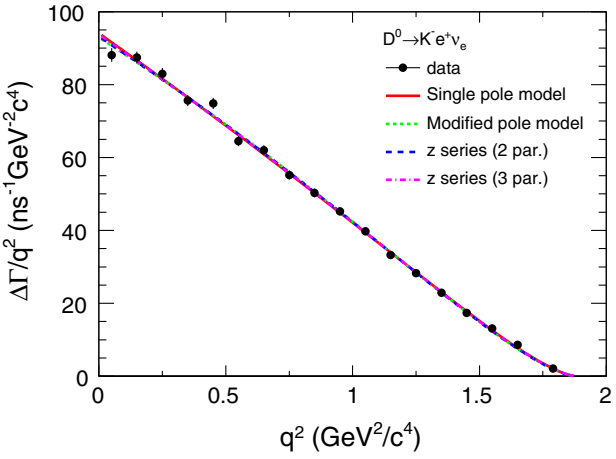

FIG. 6 (color online). Differential decay rates for $D^0 \to K^- e^+ \nu_e$ as a function of q^2. The dots with error bars show the data and the lines give the best fits to the data with different form-factor parametrizations.

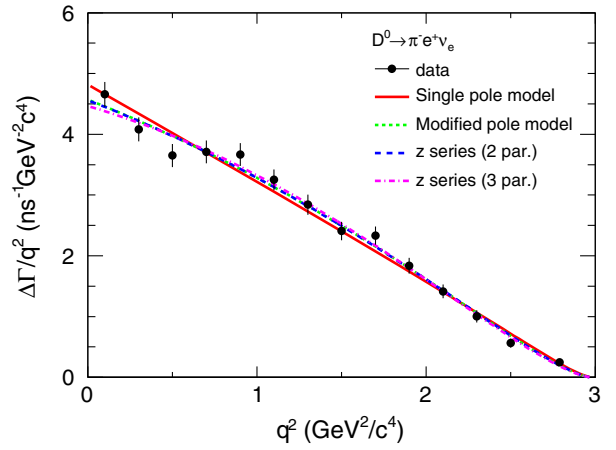

FIG. 7 (color online). Differential decay rates for $D^0 \to \pi^- e^+ \nu_e$ as function of q^2. The dots with error bars show the data and the lines give the best fits to the data with different form-factor parametrizations.

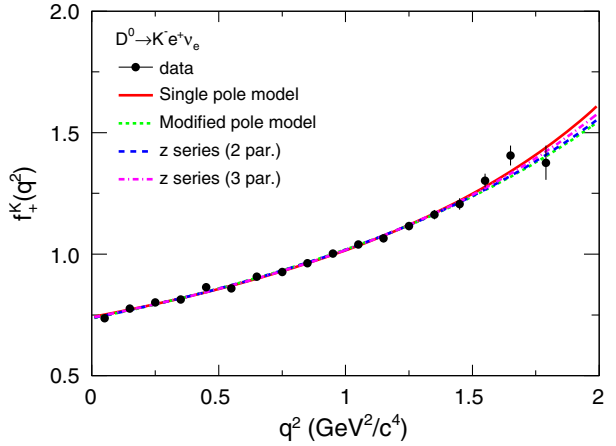

FIG. 8 (color online). Projections on $f_+^K(q^2)$ for $D^0 \to K^- e^+ \nu_e$.

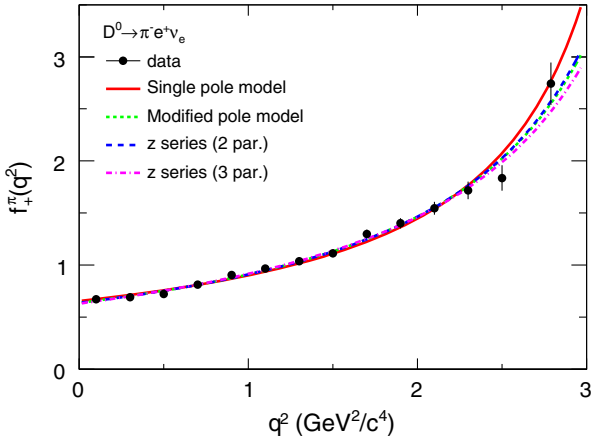

FIG. 9 (color online). Projections on $f_+^\pi(q^2)$ for $D^0 \to \pi^- e^+ \nu_e$.

in which

$$p'^3_{K(\pi)}(i) = \frac{\int_{q^2_{\min(i)}}^{q^2_{\max(i)}} p^3_{K(\pi)} |f_+^{K(\pi)}(q^2)|^2 dq^2}{|f_+^{K(\pi)}(q_i^2)|^2 (q^2_{\max(i)} - q^2_{\min(i)})}, \qquad (6.22)$$

where $|V_{cs}| = 0.97343 \pm 0.00015$ and $|V_{cd}| = 0.22522 \pm 0.00061$ are taken from the SM constraint fit [6]. In the calculation of $p'^3_{K(\pi)}(i)$, $f_+^{K(\pi)}(q^2)$ and $f_+^{K(\pi)}(q_i^2)$ are computed using the two-parameter series parametrization with the measured parameters.

E. Comparison of form-factor parameters in different parametrizations

For the single pole model, the fits give

$$M_{\text{pole}}^{D\to K} = (1.921 \pm 0.010 \pm 0.007)\ \text{GeV}/c^2, \qquad (6.23)$$

and

$$M_{\text{pole}}^{D\to \pi} = (1.911 \pm 0.012 \pm 0.004)\ \text{GeV}/c^2 \qquad (6.24)$$

for $D^0 \to K^- e^+ \nu_e$ and $D^0 \to \pi^- e^+ \nu_e$ decays, respectively. The agreement between the extracted values of pole mass and the expected values ($M_{D_{(s)}^{*+}}$) is extremely poor. For comparison, Table XIV lists the values of the pole mass $M_{\text{pole}}^{D\to K}$ and $M_{\text{pole}}^{D\to \pi}$ measured in this analysis and those previously measured at other experiments.

With the modified pole model, the fits give

$$\alpha^{D\to K} = 0.310 \pm 0.020 \pm 0.013, \qquad (6.25)$$

and

$$\alpha^{D\to \pi} = 0.279 \pm 0.035 \pm 0.011 \qquad (6.26)$$

TABLE XIV. Comparison of measurements of the pole masses $M_{\rm pole}^{D\to K}$ and $M_{\rm pole}^{D\to\pi}$.

Experiment	$M_{\rm pole}^{D\to K}$ (GeV/c^2)	$M_{\rm pole}^{D\to\pi}$ (GeV/c^2)
Mark-III [21]	$1.80^{+0.50}_{-0.20}\pm 0.25$	
E691 [32]	$2.10^{+0.40}_{-0.20}\pm 0.20$	
CLEO [33]	$2.10^{+0.40}_{-0.20}\pm 0.25$	
CLEO-II [34]	$2.00\pm 0.12\pm 0.18$	
E687 (Tag) [35]	$1.97^{+0.43}_{-0.22}\pm 0.07$	
E687 (Incl) [35]	$1.87^{+0.11}_{-0.08}\pm 0.07$	
CLEO-II [36]	$1.89\pm 0.05^{+0.04}_{-0.03}$	$1.86^{+0.10}_{-0.06}\pm 0.05$
FOCUS [37]	$1.93\pm 0.05\pm 0.03$	$1.91^{+0.15}_{-0.30}\pm 0.07$
Belle [30]	$1.82\pm 0.04\pm 0.03$	$1.97\pm 0.08\pm 0.04$
BABAR [24,25]	$1.884\pm 0.012\pm 0.015$	$1.906\pm 0.029\pm 0.023$
CLEO-c [20]	$1.97\pm 0.03\pm 0.01$	$1.95\pm 0.04\pm 0.02$
CLEO-c [38]	$1.97\pm 0.03\pm 0.01$	$1.87\pm 0.03\pm 0.01$
This work	$1.921\pm 0.010\pm 0.007$	$1.911\pm 0.012\pm 0.004$

for $D^0\to K^-e^+\nu_e$ and $D^0\to\pi^-e^+\nu_e$ decays, respectively. In the modified pole model (BK parametrization) for the form factors, $\alpha_{\rm BK}^{D\to K}$ is expected to be ∼1.75 and $\alpha_{\rm BK}^{D\to\pi}$ is expected to be ∼1.34 [20]. Our measured values of $\alpha^{D\to K}$ and $\alpha^{D\to\pi}$ significantly deviate from the values required by the modified pole model. Table XV presents a comparison of our measurements of these two parameters with those previously measured at other experiments and the expected values from the lattice QCD calculations.

F. Comparison of the measured $f_+^{K(\pi)}(q^2)$ with LQCD predictions

Figures 10(a) and 10(b) show comparisons between our measured form factors and those calculated in LQCD [26] for $D^0\to K^-e^+\nu_e$ and $D^0\to\pi^-e^+\nu_e$ semileptonic decays, respectively. From these two figures we find that, although our measured values of the form factors $f_+^K(q^2)$ and $f_+^\pi(q^2)$ are consistent within uncertainties with the LQCD predictions, our measured values of the form factors significantly deviate from the most probable values calculated in LQCD in the regions above 0.75 and 1.5 GeV^2/c^4 for $D^0\to K^-e^+\nu_e$ and $D^0\to\pi^-e^+\nu_e$ decays, respectively. The precision of the measured $f_+^K(q^2)$ and $f_+^\pi(q^2)$ is much higher than that of the LQCD calculations.

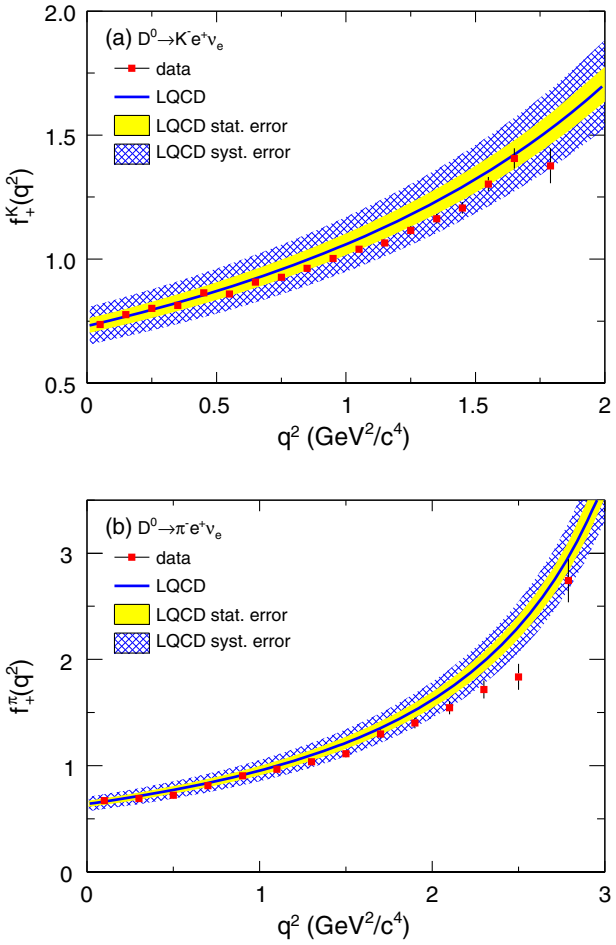

FIG. 10 (color online). Comparisons of the measured form factors (squares with error bars) with the LQCD calculations [26] (solid lines present the central values, bands present the LQCD uncertainties).

G. Comparison of measurements of $f_+^K(0)$ and $f_+^\pi(0)$

Using the measured $f_+^{K(\pi)}(0)|V_{cs(d)}|$ from the two-parameter series expansion fits, we obtain

TABLE XV. Comparison of measurements of the shape parameters $\alpha^{D\to K}$ and $\alpha^{D\to\pi}$ in the modified pole model.

Theory/experiment	$\alpha^{D\to K}$	$\alpha^{D\to\pi}$
LQCD [26]	$0.50\pm 0.04\pm 0.07$	$0.44\pm 0.04\pm 0.07$
LCSR [39]	$0.07^{+0.15}_{-0.07}$	$0.11^{+0.11}_{-0.07}$
FOCUS [37]	$0.28\pm 0.08\pm 0.07$	
Belle [30]	$0.52\pm 0.08\pm 0.06$	$0.10\pm 0.21\pm 0.10$
CLEO-c(281 pb^{-1}) (tagged) [20]	$0.21\pm 0.05\pm 0.02$	$0.16\pm 0.10\pm 0.05$
CLEO-c(281 pb^{-1}) (untagged) [38]	$0.21\pm 0.05\pm 0.03$	$0.37\pm 0.08\pm 0.03$
CLEO-c(818 pb^{-1}) [23]	$0.30\pm 0.03\pm 0.01$	$0.21\pm 0.07\pm 0.02$
BABAR [24,25]	$0.377\pm 0.023\pm 0.029$	$0.268\pm 0.074\pm 0.059$
BESIII (this work)	$0.309\pm 0.020\pm 0.013$	$0.279\pm 0.035\pm 0.011$

$$\frac{f_+^\pi(0)|V_{cd}|}{f_+^K(0)|V_{cs}|} = 0.2001 \pm 0.0026 \pm 0.0016, \quad (6.27)$$

where the first error is statistical and second systematic. With the values of $|V_{cs(d)}|$ from the SM constraint fit [6], we find

$$\frac{f_+^\pi(0)}{f_+^K(0)} = 0.8649 \pm 0.0112 \pm 0.0073, \quad (6.28)$$

where the first error is statistical and second systematic. This measured ratio, $f_+^\pi(0)/f_+^K(0) = 0.865 \pm 0.013$, is in excellent agreement with the LCSR calculation of $f_+^\pi(0)/f_+^K(0) = 0.84 \pm 0.04$ [40], but the precision is higher than the LCSR calculation by more than a factor of 3.

Using the $f_+^K(\pi)(0)|V_{cs(d)}|$ values from the two-parameter series expansion fits and taking the values of $|V_{cs(d)}|$ from the SM constraint fit [6] as inputs, we obtain the form factors

$$f_+^K(0) = 0.7368 \pm 0.0026 \pm 0.0036 \quad (6.29)$$

and

$$f_+^\pi(0) = 0.6372 \pm 0.0080 \pm 0.0044, \quad (6.30)$$

where the first errors are statistical and the second systematic.

Tables XVI and XVII show the comparisons of our measured form factors with those measured at other experiments, for which different form-factor parametrizations and values of $|V_{cs(d)}|$ have been used. Our measurements of these two form factors are consistent within errors with other measurements, but with a higher precision.

VII. EXTRACTION OF $|V_{cs}|$ AND $|V_{cd}|$

A. Determination of $|V_{cs}|$ and $|V_{cd}|$

Using the values for $f_+^{K(\pi)}(0)|V_{cs(d)}|$ from the two-parameter z-series expansion fits and in conjunction with $f_+^K(0) = 0.747 \pm 0.011 \pm 0.015$ [41] and $f_+^\pi(0) = 0.666 \pm 0.020 \pm 0.021$ [42] calculated in LQCD, we obtain

$$|V_{cs}| = 0.9601 \pm 0.0033 \pm 0.0047 \pm 0.0239 \quad (7.1)$$

and

$$|V_{cd}| = 0.2155 \pm 0.0027 \pm 0.0014 \pm 0.0094, \quad (7.2)$$

where the first uncertainties are statistical, the second ones systematic, and the third ones are due to the theoretical uncertainties in the form factor calculations.

From the measured ratio of $\frac{f_+^\pi(0)|V_{cd}|}{f_+^K(0)|V_{cs}|}$ given in Eq. (6.27) together with the LCSR calculation of $f_+^\pi(0)/f_+^K(0) = 0.84 \pm 0.04$ [40], we determine

$$\frac{|V_{cd}|}{|V_{cs}|} = 0.238 \pm 0.004 \pm 0.002 \pm 0.011, \quad (7.3)$$

where the first error is statistical, the second one systematic, and the third one is from LCSR normalization.

B. Comparison of $|V_{cs}|$ and $|V_{cd}|$

Tables XVIII and XIX give comparisons of our measured $|V_{cs}|$ and $|V_{cd}|$ with those measured at other experiments. Our measurements of $|V_{cs}|$ and $|V_{cd}|$ are of higher precision than previous results from both D meson decays and W boson decays.

TABLE XVI. Comparison of the form factor $f_+^K(0)$ measured at different experiments.

Experiment	$f_+^K(0)$	Form-factor parametrization
BES-II [17]	$0.78 \pm 0.04 \pm 0.03$	Single pole model
Belle [30]	$0.695 \pm 0.007 \pm 0.022$	Modified pole model
BABAR [24]	$0.727 \pm 0.007 \pm 0.005 \pm 0.007$	Single pole model and modified pole model
CLEO-c [23]	$0.739 \pm 0.007 \pm 0.005 \pm 0.000$	Three-parameter series expansion
BESIII (this work)	$0.7368 \pm 0.0026 \pm 0.0036$	Two-parameter series expansion

TABLE XVII. Comparison of the form factor $f_+^\pi(0)$ measured at different experiments.

Experiment	$f_+^\pi(0)$	Form-factor parametrization
BES-II [17]	$0.73 \pm 0.14 \pm 0.06$	Single pole model
Belle [30]	$0.624 \pm 0.020 \pm 0.003$	Modified pole model
CLEO-c [23]	$0.666 \pm 0.019 \pm 0.004 \pm 0.003$	Three-parameter series expansion
BABAR [25]	$0.610 \pm 0.020 \pm 0.005$	Three-parameter series expansion
BESIII (this work)	$0.6372 \pm 0.0080 \pm 0.0044$	Two-parameter series expansion

TABLE XVIII. Comparison of $|V_{cs}|$ measurements.

Experiment	$\lvert V_{cs}\rvert$	Note
PDG2014 [6]	0.986 ± 0.016	Using $D_s^+ \to \ell^+\nu_\ell$, $D^0 \to K^-\ell^+\nu_\ell$ and $D^+ \to \bar{K}^0 e^+\nu_e$
PDG2014 [6]	1.008 ± 0.021	Using $D_s^+ \to \ell^+\nu_\ell$
PDG2014 [6]	$0.953 \pm 0.008 \pm 0.024$	Using $D^0 \to K^-\ell^+\nu_\ell$ and $D^+ \to \bar{K}^0 e^+\nu_e$
PDG2014 [6]	0.97343 ± 0.00015	Global fit in the Standard Model
PDG2006 [43]	$0.94^{+0.32}_{-0.26} \pm 0.14$	Using W boson decay
BES-II [17]	$1.00 \pm 0.05 \pm 0.11$	Using $D^0 \to K^- e^+\nu_e$
CLEO-c [23]	$0.985 \pm 0.009 \pm 0.006 \pm 0.103$	Using $D^0 \to K^- e^+\nu_e$ and $D^+ \to \bar{K}^0 e^+\nu_e$
BESIII (this work)	$0.9601 \pm 0.0033 \pm 0.0047 \pm 0.0239$	Using $D^0 \to K^- e^+\nu_e$

TABLE XIX. Comparison of $|V_{cd}|$ measurements.

Experiment	$\lvert V_{cd}\rvert$	Note
PDG2014 [6]	0.225 ± 0.008	Using $D^0 \to \pi^-\ell^+\nu_\ell$, $D^+ \to \pi^0 e^+\nu_e$ and neutrino interactions
PDG2014 [6]	$0.220 \pm 0.006 \pm 0.010$	Using $D^0 \to \pi^-\ell^+\nu_\ell$ and $D^+ \to \pi^0 e^+\nu_e$
PDG2014 [6]	0.230 ± 0.011	Using neutrino interactions
PDG2014 [6]	0.22522 ± 0.00061	Global fit in the Standard Model
CLEO-c [23]	$0.234 \pm 0.007 \pm 0.002 \pm 0.025$	Using $D^0 \to \pi^- e^+\nu_e$ and $D^+ \to \pi^0 e^+\nu_e$
BESIII [44]	$0.2210 \pm 0.0058 \pm 0.0047$	Using $D^+ \to \mu^+\nu_\mu$
BABAR [25]	$0.206 \pm 0.007 \pm 0.009$	Using $D^0 \to \pi^- e^+\nu_e$
BESIII (this work)	$0.2155 \pm 0.0027 \pm 0.0014 \pm 0.0094$	Using $D^0 \to \pi^- e^+\nu_e$

TABLE XX. Comparison of $|V_{cd}|/|V_{cs}|$ measurements.

Experiment	$\lvert V_{cd}\rvert/\lvert V_{cs}\rvert$	Note
PDG2014 [6]	0.228 ± 0.009	Using $\lvert V_{cd}\rvert = 0.225 \pm 0.008$ and $\lvert V_{cs}\rvert = 0.986 \pm 0.016$
CLEO-c [23]	$0.242 \pm 0.011 \pm 0.004 \pm 0.012$	Using $D \to \pi e^+\nu_e$ and $D \to K e^+\nu_e$
BESIII (this work)	$0.238 \pm 0.004 \pm 0.002 \pm 0.011$	Using $D^0 \to \pi^- e^+\nu_e$ and $D^0 \to K^- e^+\nu_e$

Table XX gives a comparison of our measured $|V_{cd}|/|V_{cs}|$ with the one measured by CLEO-c [23] and the world average calculated with $|V_{cd}|$ and $|V_{cs}|$ given in PDG2014 [6]. Our measurement of the ratio is in excellent agreement with the world average.

VIII. SUMMARY

In summary, by analyzing about 2.92 fb^{-1} data collected at 3.773 GeV with the BESIII detector operated at the BEPCII collider, the semileptonic decays of $D^0 \to K^- e^+\nu_e$ and $D^0 \to \pi^- e^+\nu_e$ have been studied. From a total of 2793317 ± 3684 single $\bar{D}^0$ tags, 70727 ± 278 $D^0 \to K^- e^+\nu_e$ and 6297 ± 87 $D^0 \to \pi^- e^+\nu_e$ signal events are observed in the system recoiling against the single $\bar{D}^0$ tags. These yield the decay branching fractions

$$\mathcal{B}(D^0 \to K^- e^+\nu_e) = (3.505 \pm 0.014 \pm 0.033)\%$$

and

$$\mathcal{B}(D^0 \to \pi^- e^+\nu_e) = (0.295 \pm 0.004 \pm 0.003)\%.$$

Using these samples of $D^0 \to K^- e^+\nu_e$ and $D^0 \to \pi^- e^+\nu_e$ decays, we study the form factors as a function of the squared four-momentum transfer q^2 for these two decays. By fitting the partial decays rates, we obtain the parameter values for several different form-factor functions. For the physical interpretation of the shape parameters in the single pole and modified pole models, the values of the parameters obtained from our fits significantly deviate from those expected by these models. This means that the data do not support the physical interpretation of the shape parameter in those models. We choose the values of $f_+^K(0)|V_{cs}|$ and $f_+^\pi(0)|V_{cd}|$ obtained with the two-parameter series expansion as our main result. In this case, we obtain the form factors

$$f_+^K(0) = 0.7368 \pm 0.0026 \pm 0.0036$$

and

$$f_+^\pi(0) = 0.6372 \pm 0.0080 \pm 0.0044.$$

Furthermore, using the form factors calculated in recent LQCD calculations [41,42], we obtain the CKM matrix elements

$$|V_{cs}| = 0.9601 \pm 0.0033 \pm 0.0047 \pm 0.0239$$

and

$$|V_{cd}| = 0.2155 \pm 0.0027 \pm 0.0014 \pm 0.0094,$$

where the errors are dominated by the theoretical uncertainties in the form factor calculations. Our measurement of the product $f_+^K(0)|V_{cs}| = 0.7172 \pm 0.0025 \pm 0.0035$ ($f_+^\pi(0)|V_{cd}| = 0.1435 \pm 0.0018 \pm 0.0009$) is the most precise to date and would give more precise value of $|V_{cs}|$ ($|V_{cd}|$) with its precision increasing to 0.6% (1.4%) when the uncertainty of the value of the related form factor calculated in LQCD can be ignored.

Our measurements of the branching fractions, the form-factor parameters and the shapes of the form factor $f_+^{K(\pi)}(q^2)$ as a function of q^2 for $D^0 \to K^- e^+ \nu_e$ and $D^0 \to \pi^- e^+ \nu_e$ decays are all the most precise to date. These precise measurements of $f_+^K(q^2)$, $f_+^\pi(q^2)$, $f_+^K(0)$, $f_+^\pi(0)$ and $f_+^\pi(0)/f_+^K(0)$ are in good agreement with the LQCD calculations of the form factors and the LCSR calculations of the ratio of the form factors, but have higher precision than those calculated in theories based on QCD, and therefore will allow incisive tests of any future theoretical calculations.

ACKNOWLEDGMENTS

The BESIII collaboration thanks the staff of BEPCII and the IHEP computing center for their strong support. This work is supported in part by National Key Basic Research Program of China under Contracts No. 2009CB825204, No. 2015CB856700; National Natural Science Foundation of China (NSFC) under Contracts No. 10935007, No. 11125525, No. 11235011, No. 11322544, No. 11335008, No. 11425524; the Chinese Academy of Sciences (CAS) Large-Scale Scientific Facility Program; Joint Large-Scale Scientific Facility Funds of the NSFC and CAS under Contracts No. 11179007, No. U1232201, No. U1332201; CAS under Contracts No. KJCX2-YW-N29, No. KJCX2-YW-N45; 100 Talents Program of CAS; INPAC and Shanghai Key Laboratory for Particle Physics and Cosmology; German Research Foundation DFG under Collaborative Research Center Contract No. CRC-1044; Istituto Nazionale di Fisica Nucleare, Italy; Ministry of Development of Turkey under Contract No. DPT2006K-120470; Russian Foundation for Basic Research under Contract No. 14-07-91152; U.S. Department of Energy under Contracts No. DE-FG02-04ER41291, No. DE-FG02-05ER41374, No. DE-FG02-94ER40823, No. DESC0010118; U.S. National Science Foundation; University of Groningen (RuG) and the Helmholtzzentrum fuer Schwerionenforschung GmbH (GSI), Darmstadt; Institute for Basic Science, Korea, Project Code IBS-R016-D1; the Swedish Research Council.

[1] N. Cabibbo, Phys. Rev. Lett. **10**, 531 (1963).
[2] M. Kobayashi and T. Maskawa, Prog. Theor. Phys. **49**, 652 (1973).
[3] G. Rong, Chin. Phys. C **34**, 788 (2010); G. Rong, Y. Fang, H. L. Ma, and J. Y. Zhao, Phys. Lett. B **743**, 315 (2015).
[4] M. Ablikim *et al.* (BESIII Collaboration), Nucl. Instrum. Methods Phys. Res., Sect. A **614**, 345 (2010).
[5] C. Zhang (BEPC & BEPCII Teams), Performance of the BEPC and progress of the BEPCII, in *Proceedings of APAC, Gyeongju, Korea, 2004*, pp. 15–19.
[6] K. A. Olive *et al.* (Particle Data Group), Chin. Phys. C **38**, 090001 (2014).
[7] T. Becher and R. J. Hill, Phys. Lett. B **633**, 61 (2006).
[8] D. Becirevic and A. B. Kaidalov, Phys. Lett. B **478**, 417 (2000).
[9] J. G. Körner and G. A. Schuler, Z. Phys. C **38**, 511 (1988); Phys. Lett. B **226**, 185 (1989); Z. Phys. C **46**, 93 (1990); J. G. Körner, K. Schilcher, M. Wirbel, and Y. L. Wu, Z. Phys. C **48**, 663 (1990).
[10] M. Wirbel, B. Stech, and M. Bauer, Z. Phys. C **29**, 637 (1985); M. Bauer and M. Wirbel, Z. Phys. C **42**, 671 (1989).
[11] C. G. Boyd, B. Grinstein, and R. F. Lebed, Nucl. Phys. **B461**, 493 (1996).
[12] N. Isgur and M. B. Wise, Phys. Lett. B **232**, 113 (1989); **237**, 527 (1990); E. Eichten and B. Hill, Phys. Lett. B **234**, 511 (1990); H. Georgi, Phys. Lett. B **240**, 447 (1990).
[13] S. Agostinelli *et al.* (GEANT4 Collaboration), Nucl. Instrum. Methods Phys. Res., Sect. A **506**, 250 (2003).
[14] Z. Y. Deng *et al.*, Chin. Phys. C **30**, 371 (2006).
[15] S. Jadach, B. F. L. Ward, and Z. Was, Comput. Phys. Commun. **130**, 260 (2000).
[16] D. J. Lange, Nucl. Instrum. Methods Phys. Res., Sect. A **462**, 152 (2001); R.-G. Ping, Chin. Phys. C **32**, 599 (2008).
[17] M. Ablikim *et al.* (BES Collaboration), Phys. Lett. B **597**, 39 (2004).
[18] M. Ablikim *et al.* (BES Collaboration), Phys. Lett. B **603**, 130 (2004); **608**, 24 (2005); **610**, 183 (2005).
[19] H. Albrecht *et al.* (ARGUS Collaboration), Phys. Lett. B **241**, 278 (1990).
[20] J. Y. Ge *et al.* (CLEO Collaboration), Phys. Rev. D **79**, 052010 (2009).
[21] J. Adler *et al.* (Mark-III Collaboration), Phys. Rev. Lett. **62**, 1821 (1989).

[22] F. Butler *et al.* (CLEO Collaboration), Phys. Rev. D **52**, 2656 (1995).
[23] D. Besson *et al.* (CLEO Collaboration), Phys. Rev. D **80**, 032005 (2009).
[24] B. Aubert *et al.* (*BABAR* Collaboration), Phys. Rev. D **76**, 052005 (2007).
[25] J. P. Lees *et al.* (*BABAR* Collaboration), Phys. Rev. D **91**, 052022 (2015).
[26] C. Aubin *et al.* (Fermilab Lattice Collaboration, MILC Collaboration, and HPQCD Collaboration), Phys. Rev. Lett. **94**, 011601 (2005).
[27] A. Abada, Nucl. Phys. **B619**, 565 (2001).
[28] P. Ball, V. M. Braun, and H. G. Dosch, Phys. Rev. D **44**, 3567 (1991).
[29] W. Y. Wang, Y. L. Wu, and M. Zhong, Phys. Rev. D **67**, 014024 (2003).
[30] L. Widhalm *et al.* (Belle Collaboration), Phys. Rev. Lett. **97**, 061804 (2006).
[31] M. Lefebvre, R. K. Keeler, R. Sobie, and J. White, Nucl. Instrum. Methods Phys. Res., Sect. A **451**, 520 (2000).
[32] J. C. Anjos *et al.* (E691 Collaboration), Phys. Rev. Lett. **62**, 1587 (1989).
[33] G. Crawford *et al.* (CLEO Collaboration), Phys. Rev. D **44**, 3394 (1991).
[34] A. Bean *et al.* (CLEO Collaboration), Phys. Lett. B **317**, 647 (1993).
[35] P. L. Frabetti *et al.* (E687 Collaboration), Phys. Lett. B **364**, 127 (1995).
[36] G. S. Huang *et al.* (CLEO Collaboration), Phys. Rev. Lett. **94**, 011802 (2005).
[37] J. M. Link *et al.* (FOCUS Collaboration), Phys. Lett. B **607**, 233 (2005).
[38] S. Dobbs *et al.* (CLEO Collaboration), Phys. Rev. D **77**, 112005 (2008).
[39] T. M. Aliev, V. L. Eletsky, and Y. I. Kogan, Sov. J. Nucl. Phys. **40**, 527 (1984).
[40] P. Ball, Phys. Lett. B **641**, 50 (2006).
[41] H. Na, C. T. H. Davies, E. Follana, G. P. Lepage, and J. Shigemitsu (HPQCD Collaboration), Phys. Rev. D **82**, 114506 (2010).
[42] H. Na, C. T. H. Davies, E. Follana, J. Koponen, G. P. Lepage, and J. Shigemitsu (HPQCD Collaboration), Phys. Rev. D **84**, 114505 (2011).
[43] W. M. Yao *et al.* (Particle Data Group), J. Phys. G **33**, 1 (2006).
[44] M. Ablikim *et al.* (BESIII Collaboration), Phys. Rev. D **89**, 051104(R) (2014).